THE ROLE OF SYN-EXTENSIONAL LAMPROPHYRE MAGMATISM IN CRUSTAL DYNAMICS – THE CASE OF THE MENDERES METAMORPHIC CORE COMPLEX, WESTERN TURKEY

Sebastian FISCHER[1], Dejan PRELEVIĆ[1,2], Cüneyt AKAL[3], Rolf L. ROMER[4], Axel Gerdes[5]

[1]Institute of Geosciences, University of Mainz, Becherweg 21, D-55099 Mainz, Germany
[2]Faculty of Mining and Geology, University of Belgrade, Djušina 7, 11000 Belgrade, Serbia
[3]Dokuz Eylül Üniversitesi, Mühendislik Fakültesi, Jeoloji Mühendisliği Bölümü, Tr-35397 Buca, Izmir, Turkey
[4]Deutsches GeoForschungsZentrum (GFZ), Telegrafenberg, D-14473 Potsdam, Germany
[5]Goethe-Universität Frankfurt Institut für Geowissenschaften Petrologie und Geochemie Altenhöferallee 1, 60438 Frankfurt, Germany

ABSTRACT

The Menderes Massif in Turkey represents one of the largest metamorphic core complexes in the world. It is regarded as a section of lower continental crust exhumed along low-angle detachment faults in the Late Miocene during a period of extension that affected the entire Aegean province. Syn-extensional magmatic activity within the Menderes metamorphic core complex is predominantly felsic forming several plutons, whereas mantle-derived magmatism has not been known so far. Here, we present a detailed study of the petrology and geochemistry of previously unreported mafic to intermediate lamprophyres within the Menderes Massif and assess their role in the geodynamic evolution of the core complex.

The Menderes lamprophyres are mostly kersantites, with 49 – 60 wt% SiO_2, 3.2 – 8.4 wt% MgO, 100 – 360 ppm Cr, 32 – 132 ppm Ni, and Mg# of 37 – 50. Positive Pb and negative Ti-Nb-Ta anomalies suggest a clear orogenic affinity. Isotopes of Sr and Pb are relatively radiogenic ($^{87}Sr/^{86}Sr$ = 0.70609 – 0.71076; $^{206}Pb/^{204}Pb$ = 18.88 – 19.03, $^{207}Pb/^{204}Pb$ > 15.71), while Nd is unradiogenic (εNd = -1.4 – -3.2). Most phenocrysts are sharply zoned with a primitive core (Mg# 77 – 85, up to 0.95 wt% Cr_2O_3 in clinopyroxene; Mg# 72 – 76 in amphibole) and a more evolved rim (Mg# 68 – 74, < 0.25 wt% Cr_2O_3 in clinopyroxene; Mg# 69 – 71 in amphibole). Trace element ratios between different cores may vary significantly (e.g. Dy/Yb 2 – 5 in amphiboles), whereas rims show less variation but are more enriched than the cores.

U-Pb dating of zircons provides an age of 15 Ma for the lamprophyres, coeval with the syn-extensional granite magmatism. The Hf isotopic composition of magmatic zircons is variably unradiogenic ($^{176}Hf/^{177}Hf_{15Ma}$ = 0.28248 – 0.28253, εHf_{15Ma} = -8.6 – -10.5), while zircon xenocrysts with dominantly Cadomian and older ages show highly variable Hf isotopic signatures at the time of lamprophyre emplacement (εHf_{15Ma} = -7.6 – -46.7).

The orogenic geochemical signature of the lamprophyres' parental melts is similar to nearby orogenic lavas from the W. Anatolian volcanic province. Variation in bulk-rock εNd and in Dy/Yb ratios of phenocryst cores reflect moderate mantle heterogeneity. The chemical heterogeneity of phenocrysts and zircon εHf values implies intense hybridisation of proto-lamprophyre melts with felsic crustal melts, most probably derived from the melting of augen gneisses of the Menderes basement. We propose that fluid released from the lamprophyre primary melt had a decisive impact on crustal melting and the formation of granitic plutons within the Menderes core complex.

INTRODUCTION

Metamorphic core complexes are the result of intense extensional tectonics within the continental lithosphere. They are dome-shaped structures of lower and middle-crustal lithologies

exposed at the surface along low-angle normal (detachment) faults, forced by the extension-assisted diapiric ascent of partially molten crust along localised zones of high-strain ductile deformation (Crittenden *et al.*, 1978, Lister & Davis, 1989). The generation and role of mantle-derived melts in crustal dynamics and the formation of metamorphic core complexes remain controversial (Amato & Miller, 2004, Miller *et al.*, 1992) due to the small number of occurrences where synchronous mantle-derived magmatism has been observed (Konstantinou *et al.*, 2013). In a synergy of several processes, mantle-derived magmatism may potentially be one of the major driving forces in the generation of core complexes, triggering thermomechanical weakening, partial melting, mobilisation of rheologically weakened parts of the solid crust and crustal flow in its lower parts.

The Menderes Massif represents one of the largest metamorphic core complexes in the world and is the most prominent geomorphological feature in Western Anatolia, Turkey (e.g. Şengör et al, 1984; Bozkurt & Mittwede, 2001; Hetzel *et al.*, 1995; Işık *et al.*, 2004; Okay, 2001). The massif consists of a core of late Precambrian metagranites (augen gneisses) that are juxtaposed against Palaeozoic to Palaeocene metasedimentary rocks forming a lower grade metamorphic envelope around the high-grade metagranites (Okay, 2001). Several models have been proposed to explain the extensional regime that led to the exhumation of the Menderes metamorphic core complex, including tectonic escape, back-arc extension triggered by slab rollback, orogenic collapse, and transtensional tectonics across the West Anatolia Transfer Zone (Çemen *et al.*, 2006; Gessner *et al.*, 2013 and references therein). Extension commenced in the Late Oligocene (Çemen et al., 2006) or Early to Middle Miocene (Yılmaz et al., 2000) and was characterised by syn-extensional magmatism in close association with ductile shear zones and north- or south-facing detachment faults. Syn-extensional intrusions dominantly include felsic magmatic rocks, with Salihli and Turgutlu situated in the central submassif, and Egrigöz in the northern submassif (Erkül *et al.*, 2013; Erkül, 2012; Erkül & Erkül, 2012; Ersoy *et al.*, 2008; Hasozbek *et al.*, 2010). The granites have metaluminous/peraluminous and high-K calc-alkaline character being interpreted as transitional between I- and S-type (Erkül *et al.*, 2013). Simultaneous to granitic plutonism, a wider

area in West Anatolia is characterised by basaltic ultrapotassic and calc-alkaline volcanic activity, ultimately interpreted to be derived from a delaminated metasomatised lithospheric mantle (Ersoy & Palmer, 2013; Ersoy *et al.*, 2017; Ersoy & Helvaci, 2007; Prelević *et al.*, 2012; Soder *et al.*, 2016).

In this paper, we report for the first time the occurrence of mafic intrusive rocks from the central parts of the Menderes metamorphic core complex. Our comprehensive study of several lamprophyric sill-like intrusions of mafic to intermediate composition includes detailed geological and petrological observations, as well as whole-rock geochemical, and new zircon U-Pb age and Hf isotope data. We show that these volumetrically minor, hydrous mantle-derived intrusions were emplaced simultaneously with syn-extensional granitic magmas into the overthickened Menderes crust. The lamprophyres show a broad compositional range, from primitive mafic to more evolved intermediate compositions, with the most felsic sills approaching the compositions of nearby Miocene granites. These features, in combination with the presence of coeval granitic magmatism, set up a perfect ground for a detailed study of the role of lamprophyric melts in hydrous mantle-crust interaction during the formation of metamorphic core complexes. We present a holistic study of the petrogenesis of the lamprophyric magma within the Menderes metamorphic core complex and discuss the significance of fluid-laden alkaline magma formation in the mantle for the origin of the core complex in general.

REGIONAL GEOLOGICAL SETTING

The geological evolution of Turkey shares the complexity of the whole Mediterranean area that is characterised by the closure of the Tethyan ocean(s) and the amalgamation of various continental fragments during the Alpine orogeny (Şengör & Yılmaz, 1981). The largest and most prominent unit in the Eastern Mediterranean is the Anatolide-Tauride block in the southern part of Turkey. The Palaeozoic stratigraphy of the Anatolide-Tauride block is similar to that of the Arabian Platform, from which it is separated by the Assyrian-Zagros Suture. Due to stratigraphic similarity, the Anatolide-Tauride block is generally regarded as part of the Gondwana continent (Okay &

Tuysuz, 1999). To the north of the Anatolide-Tauride block, there are the Pontides that from west to east comprise the Strandja, the Istanbul, and the Sakarya zones, all of which are regarded as having a Laurasian affinity (Okay & Nikishin, 2015). The Istanbul and Sakarya zones are separated by the Intra-Pontide Suture, which probably represents a branch of the Neotethys (Okay et al., 2001). The boundary between the Pontides and the Anatolide-Tauride block is defined by the Izmir-Ankara-Erzincan Suture Zone, which represents the position of the main Neotethyan ocean and marks the boundary between the northern (Laurasian) and the southern (Gondwanan) parts of Turkey (e.g. Okay et al., 2001; Robertson & Ustaömer, 2009 and references therein).

The tectonic setting of Western Turkey changed in the Late Oligocene from compression to extension (Çemen *et al.*, 2006 and references therein), which in Early and Middle Miocene resulted in widespread, dominantly calc-alkaline magmatism that changed in the Late Miocene gradually to more alkaline compositions (Agostini *et al.*, 2007; Aldanmaz et al., 2000; Altunkaynak & Dilek, 2006). In the Menderes metamorphic core complex, tectonic activity is controlled by active subduction in the Hellenic and Cyprus subduction zones that have been active since the Middle Jurassic (van Hinsbergen *et al.*, 2005). Seismic models show an irregular geometry of the subducted slab under Western Anatolia due to rollback, tearing, and windowing (Biryol *et al.*, 2011; Wortel & Spakman, 2000; Bocchini *et al* ., 2018).

MENDERES METAMORPHIC CORE COMPLEX: CENOZOIC EXTENSIONAL DEFORMATION

The Menderes metamorphic core complex is one of the most prominent geomorphological features in Western Anatolia (Figure 1). It represents the westernmost expression of the extending portion of the Alpine-Himalayan belt in Turkey (e.g. Sengör, 1984; Okay, 2001; Bozkurt & Mittwede, 2001). It consists of a core of Precambrian (Cadomian) metagranites (also referred to as

augen gneiss, orthogneiss, or augen schist) with minor units of intercalated high-grade rocks including eclogites (Candan et al. 2001). The core is overlain by a cover series of Palaeozoic to Palaeocene metasedimentary rocks (Okay, 2001). The Cadomian basement and its sedimentary cover sequences were affected by Eocene regional metamorphism related to the closure of the Neotethys and the collision of the Anatolide-Tauride block with the Pontides in the north (Collins & Robertson, 1999; Hetzel & Reischmann, 1996; Lips *et al.*, 2001). The collisional regime led to imbrication and southward thrusting of the Lycian Nappes over the Menderes metamorphic core complex (Rimmelé *et al.*, 2003), possibly increasing the crustal thickness to 60 km (Bozkurt & Oberhänsli, 2001; Rimmelé *et al.*, 2003; Şengör *et al.*, 1985). Transition to an extensional regime commenced in the Late Oligocene (Çemen *et al.*, 2006; Dewey & Şengör, 1979) or Early to Middle Miocene as indicated by the development of horst-graben systems (Yılmaz *et al.*, 2000). This finally led to the gradual exhumation and erosion of the Menderes metamorphic core complex, which brought the overthickened crust to a thickness of 28 – 35 km (Doğru *et al.*, 2018; Makris & Stobbe, 1984; Zhu *et al.*, 2006).

MIOCENE MAGMATISM IN THE MENDERES METAMORPHIC CORE COMPLEX

In the broader area of the Menderes metamorphic core complex, Miocene magmatism is dominated by granitic intrusions with several plutonic bodies emplaced within the core and the cover series, intruding the footwall of low-angle normal faults that form the contact between the metamorphic units and the structurally overlying Neogene sediments (Bozkurt & Mittwede, 2001; Glodny & Hetzel, 2007). These intrusions are mostly felsic, with the most prominent being the Salihli and Turgutlu granitoids (Figure 1) (Catlos *et al.*, 2010; Oner *et al.*, 2010). Their compositions range from granodioritic to leucogranitic. Their age of 15 Ma has been interpreted as being syn-tectonic to the exhumation of the Menderes Massif (Hetzel *et al.*, 1995).

Only a few small intrusions of mafic to intermediate magmatic rocks have been shortly reported for the central Menderes Massif (Akal, 1993; Fischer *et al.*, 2010), and a more extensive

study is the subject of the present contribution. This mafic magmatism is part of the widespread extension-related high-K calc-alkaline and ultrapotassic magmatism of Early and Middle Miocene age in Western Anatolia (e.g. Aldanmaz *et al.*, 2000; Altunkaynak & Dilek, 2006; Ersoy & Palmer, 2013; Prelević *et al.*, 2015). The Menderes mafic rocks are lamprophyres, occurring as sills and dykes of variable dimensions, typically oriented (sub-)parallel to the foliation of the metapsammitic country rocks of the cover series (Figure 2a, b). The thickness of the sills ranges from 50 cm to more than 30 m and their lateral extent ranges from a few metres to several hundred metres (Supplementary dataset 1). Although no chilled margins were found, the sills always have sharp contacts with their host rocks. They internally show thin shells of spheroidal exfoliation due to weathering (Figure 2c). All sills contain variable amounts of entrained material (xenoliths and xenocrysts). One sill shows a feeding dyke at one end of the intrusion. The dyke cross-cuts the foliation of the country-rock and contains far more xenoliths and xenocrysts than the sill. Nine different intrusive bodies have been sampled (Figure 2; Table 1).

METHODS

Whole-rock major (SiO_2, Al_2O_3, Fe_2O_3(t), MnO, MgO, CaO, Na_2O, K_2O, TiO_2, P_2O_5, SO_3, Cr_2O_3, NiO) and trace (Ba, Ce, Co, Cr, Cs, Cu, Ga, La, Nb, Nd, Ni, Pb, Pr, Rb, Sc, Sm, Sr, Th, U, V, W, Y, Zn, Zr) elements were measured on fused discs and powder press tablets, respectively. Measurements were performed routinely on a Philips MagiX Pro at the Institute of Geosciences at the University of Mainz (Supplementary dataset 2). Trace element analysis (including REE) was performed on glass beads produced from whole-rock powder diluted with MgO and melted on an iridium strip heater (Nehring *et al.*, 2008; Stoll *et al.*, 2008). The measurements were carried out on a New Wave Research UP-213 laser ablation unit (213 nm wavelength, Nd:YAG laser) coupled to an Agilent 7500ce Quadrupole ICP-MS at the Institute of Geosciences at the University of Mainz. NIST SRM 612 was used as an external standard using the values of Pearce *et al.* (1997). The Ca concentration as determined by XRF analysis served as an internal standard. The basaltic glass

BCR-2G was measured regularly to check data quality using the values given in the GeoReM online database (Jochum *et al.*, 2005). BCR-2G values could be reproduced usually within 10 %, except for V, Rb, U (within 15 %) and Cr, Mn, Ni, Cs, Pb (>15 %) (Supplementary dataset 2). The following isotopes were analysed by LA-ICP-MS measurements (detection limits in parentheses, ppb): ^{7}Li (47), ^{45}Sc (75), ^{47}Ti (451), ^{51}V (29), ^{60}Ni (183), ^{85}Rb (29), ^{88}Sr (24), ^{89}Y (24), ^{90}Zr (45), ^{93}Nb (23), ^{133}Cs (19), ^{137}Ba (164), ^{139}La (20), ^{140}Ce (18), ^{141}Pr (17), ^{146}Nd (106), ^{147}Sm (130), ^{153}Eu (34), ^{157}Gd (125), ^{163}Dy (82), ^{165}Ho (21), ^{166}Er (64), ^{172}Yb (97), ^{175}Lu (22), ^{178}Hf (72), ^{181}Ta (22), ^{232}Th (26), ^{238}U (18).

Strontium, Nd, and Pb isotope analyses were carried out at the GFZ German Research Centre for Geosciences (Potsdam). Samples were dissolved in screw-top beakers using concentrated HF on a hotplate for four days at 160 °C. The digested samples were dried. Fluorides were destroyed by redissolving samples in 2 N HNO_3 and evaporating the acid. The dried samples were taken up in HCl for ion exchange chemistry. A detailed description of the analytical method is given in Prelević et al. (2008). The Nd and Pb isotopic compositions were measured on a Finnigan MAT 262 using dynamic multi-collection and static multi-collection, respectively, the Sr isotopic compositions were measured on a Thermo Fisher Scientific Triton using dynamic multi-collection. During the measurement period, NBS-987 Sr-reference material and the La Jolla Nd-standard yielded average $^{87}Sr/^{86}Sr$ and $^{143}Nd/^{144}Nd$ values of 0.710270 ± 14 (2σ, N = 18) and 0.511850 ± 7 (2σ, N = 11), respectively. Lead isotope data were corrected for instrumental fractionation with 0.1% per atomic mass units (a.m.u.) as determined from the long-term reproducibility of Pb reference material NBS-981. The accuracy and precision of reported Pb isotope ratios are better than 0.1% at the 2σ level of uncertainty.

Major element composition of minerals was determined on polished thin sections using a JEOL SuperProbe JXA8900 RL at the Institute of Geosciences at the University of Mainz, using 15kV acceleration voltage, 12 nA beam current, and 2 µm beam diameter. A set of natural and

synthetic standards was used for calibration (Supplementary dataset 2). Data reduction was performed using the φρZ method (Pouchou & Pichoir, 1984).

The trace element contents of the same clinopyroxene, amphibole and phlogopite grains measured by microprobe were determined by LA-ICP-MS using the same setup as for the whole rock trace element contents (Supplementary dataset 2). A New Wave Research 193 laser ablation unit (193 nm wavelength, excimer laser) was used for the ablation of the minerals. The data were processed using the freeware PEPITA (Dunkl *et al.*, 2008).

The U-Pb age of zircon and monazite and the Hf isotopic composition of zircon were determined at the LA-ICP-MS laboratory of the Earth Sciences Department at the University of Frankfurt. Zircon was extracted by standard separation techniques and was mounted in epoxy tablets and polished to expose their inner structure (Supplementary dataset 3). About 100 zircon grains were analysed. CL (cathodoluminescence) images were obtained using JEOL SuperProbe JXA8900 RL at the Institute of Geosciences at the University of Mainz. Sample ablation for U-Th-Pb analysis was performed with a Resolution M50 193 nm ArF Excimer laser system (Resonetics) using a 17-23 □m (5 Hz, 4 J cm^{-2}) spot and a Thermo Scientific Element 2 ICP-MS instrument following the methods described by (Gerdes & Zeh, 2006). Data processing (including common lead correction) was performed using Isoplot (Ludwig, 2003) - supported by in-house developed Microsoft Excel-based spreadsheets. The accuracy of the U-Th-Pb method was verified by analyses of reference zircon materials 91500 and Plešovice. Sample ablation for Lu-Hf isotope analysis was performed using the same laser system using a 28-40 □m spot (5 Hz, 7 J cm^{-2}) and a Thermo Fisher Scientific Neptune multi-collector ICP-MS, following the methods described by Gerdes & Zeh (2006) and Zeh *et al.* (2007). Hf isotope data were adjusted relative to the JMC475 of $^{176}Hf/^{177}Hf$ ratio = 0.282160 and the quoted uncertainties are quadratic additions of the within run precision of each analysis and the reproducibility of the JMC475 (2 SD = 0.0028%, n = 8). Accuracy and external reproducibility of the Lu-Hf method was verified by repeated analyses of reference zircon materials GJ-1 and Plešovice, respectively.

RESULTS

PETROGRAPHY OF LAMPROPHYRES FROM THE MENDERES METAMORPHIC CORE COMPLEX

According to IUGS classification (Le Maitre, 2002; Rock, 1991; Wimmenauer, 1973; Woolley *et al.*, 1996), lamprophyres are melanocratic hypabyssal igneous rocks with microporphyritic textures carrying (hydrous) mafic phenocrysts. Feldspar and other felsic minerals are restricted to the groundmass. Calc-alkaline or shoshonitic lamprophyres received their group name from the common association with calc-alkaline granitic rocks (Rock, 1977), and consist entirely of feldspar-bearing varieties, excluding glassy, carbonate- and feldspathoid-dominated lamprophyres.

The Menderes lamprophyres are mesocratic, fine- to medium-grained and typically porphyritic with phlogopite as dominant, and pyroxenes and amphiboles as minor phenocrystic phases, in a groundmass of plagioclase with minor quartz and alkali-feldspar together with fine-grained crystals of the phenocrystic phases. Calcite may occur as a groundmass phase in some samples. Accessory phases are apatite (usually as inclusions in other minerals) and oxides (most commonly ilmenite) and a few samples contain amoeboid pyrite. Based on their mineralogy (dominant hydrous phases, feldspar(s) restricted to groundmass, porphyritic, mesocratic), geochemistry (high contents of alkali elements, large-ion lithophile elements, and P, see below) and field appearance (intruded as dykes/sills), the Menderes mafic intrusions studied here classify as kersantite and less commonly as spessartite. For simplicity, we refer to them as lamprophyres hereafter.

Dark mica (phlogopite and biotite) is the most abundant phenocryst and forms subhedral to anhedral crystals that are up to 1 mm in size (Figure 3a), reddish-brown and optically unzoned. Clinopyroxene is the second most common phenocryst forming 100 – 300 μm large anhedral to euhedral grains. The sub- to anhedral grains typically form clusters that are isolated or associated with calcite or quartz (xeno)crysts (Figure 3e – 3h). In the latter case, there is always a thin layer of

alkali feldspar between the clinopyroxene rim and quartz. Back-scattered electron (BSE) images reveal concentric zonation for most clinopyroxene crystals. Some clinopyroxene grains, however, show patchy zoning (Figure 3c). Orthopyroxene is relatively rare as a phenocrystic phase, forming subhedral to euhedral grains (100 – 300 μm) and is typically concentrically zoned. Orthopyroxene commonly shows alteration along fractures (Figure 3c). Red-brown amphibole is an abundant phase and forms up to 500 μm large distinctly zoned (optically and in BSE images) crystals with a homogeneous core and a 50 – 100 μm wide, homogenous rim (Figure 3b). The contact between the two zones is always sharp. The groundmass typically consists of sub- to euhedral plagioclase (< 200 □m) with minor alkali feldspar and quartz (<100 pm) (Figure 3d).

All samples show signs of alteration in the form of veins, finely dispersed material throughout the thin section and replacement textures around phenocrysts. Distinct replacement textures interpreted as pseudomorphs after olivine (iddingsite) occur in the most Mg-rich samples (Supplementary dataset 4).

Xenocrysts and xenoliths occur in all sampled sills but to a different extent. Up to 1 cm large rounded quartz aggregates are common. The xenoliths tend to be accumulated near the margins of the sills and are particularly abundant in the feeding dyke of sill number 3. There are granitic (augen gneiss – sample 10-MEN-61x), gabbro-like, calc-silicate (sample 10-MEN-62) and impure quartzite and metapsammite xenoliths (samples 10-MEN-56, 10-MEN-59 and 10-MEN-72). Importantly, the augen gneiss xenoliths are widespread and most numerous and demonstrate either partial melting or partial consumption by the lamprophyric magma, the processes that were impossible to differentiate further.

MINERAL CHEMISTRY

Major and trace element compositions were analysed on the same mineral grains in two thin sections from sill 9 (Figure 2), which seem to be petrographically representative for the entire magmatic suite. Moreover, minerals in this sill are sufficiently coarse-grained to obtain core and rim compositions of individual grains by LA-ICP-MS at reasonable spot sizes. The mineral composition

data, some diagrams and BSE images of the analysed grains are provided in Supplementary datasets 5, 6, 7 and 9.

Amphibole

Amphibole phenocrysts demonstrate pronounced optical core-rim zonation (Figure 3b) that is reflected in the chemical composition (Figure 4a). There is a sharp drop in Al_2O_3 contents (11.9 – 12.9 wt% in cores to 10.0 – 10.7 wt% in rims) as well as MgO and FeO contents (Mg# of 72 – 76 in the cores and 69 – 72 in the rims). CaO concentrations are invariable with values around 11 wt%, whereas TiO_2 contents are higher in the rims (~ 4 wt%) than in the cores (~ 3 wt%). The Cr_2O_3 content in the core (~ 0.2 wt%) tends to increase slightly towards the contact to the rim zone and then decreases outward through the rim.

The contents of trace elements differ between cores and rims. The rims are enriched in most trace elements (e.g. La core 7 – 13 ppm vs. La rim 23 – 53 ppm; Figure 5). Although spidergram patterns for cores and rims are broadly similar (Supplementary dataset 4b), trace element ratios differ (Figure 6). For example, Dy/Yb and Eu* from cores vary significantly (2.2 – 4.7 and 0.62 – 0.94, respectively), whereas the same ratios from rims vary much less (Dy/Yb 2.4 – 3.3 and Eu/Eu* 0.57 – 0.67). The rims show a distinct negative Eu-anomaly (Eu/Eu*), whereas a corresponding anomaly is less pronounced or absent in the cores (Figure 6).

Clinopyroxene

Clinopyroxene phenocrysts are diopsidic augite and can be subdivided into three petrographic groups. Group I includes solitary crystals with a primitive core (Mg# 77 – 85, Cr_2O_3 up to 0.95 wt%) and a more evolved rim (Mg# 68 – 74, Cr_2O_3 0.07 – 0.25 wt%). Locally, there are two zones around the primitive core, an intermediate zone that is compositionally less evolved than the outermost rim (e.g. Figure 4b). Core and rim compositions of solitary clinopyroxene phenocrysts fall in two distinct populations, separated by a gap in Mg#, as demonstrated in the Mg# vs. Cr_2O_3 diagram (Supplementary dataset 5a). Similar to amphibole, Group I clinopyroxene rims show a significantly more enriched REE pattern than the cores and display a pronounced Eu-

anomaly, which is small or absent in the cores. Trace element ratios are comparable to those of amphibole (Figure 6), with a significant range among cores (e.g. Dy/Yb 2.1 – 3.4) and less variation among rims (Dy/Yb 2.0 – 2.4). Group II clinopyroxene is chemically indistinguishable from Group I clinopyroxene, but differs petrographically, in that the grains have patchy BSE patterns (Figure 3c). The major element compositions of dark and bright BSE areas correspond to the compositions of cores and rims of Group I clinopyroxene. In terms of trace element concentrations, Group II clinopyroxene overlaps with the rim compositions of Group I clinopyroxene but shows a greater range. Group III comprises (late-stage) clinopyroxene that formed around carbonate and quartz xenocrysts, respectively. Clinopyroxene grains around carbonate xenocrysts can have high Mg# comparable to solitary clinopyroxene of Group I (and Group II), although their Cr_2O_3 content is similar to rims of Group I and II. Group III clinopyroxene grains are zoned and generally more evolved (Mg# 58 – 78, Cr_2O_3 < 0.15 wt%) than Group I and II clinopyroxene. There is no distinct chemical difference between their cores and rims (Supplementary dataset 5a).

IN SITU ZIRCON U-Pb GEOCHRONOLOGY AND Hf ISOTOPE ANALYSES

More than one hundred zircon and a few monazite grains were extracted from three lamprophyre samples (10-MEN-50, 10-MEN-68, 10-MEN-71) and one grus sample collected immediately adjacent to the largest sill. Many of the zircon grains from the lamprophyres are inherited or assimilated, with rounded shapes (Supplementary dataset 3). These grains yield Archaean, Proterozoic, or Pan-African ages (Supplementary datasets 8a (inset), and 11). Less abundant magmatic zircon is euhedral, elongate, shows oscillatory zoning, and yields a U-Pb age of 15.02 ± 0.22 Myr (Supplementary dataset 8a). Seven monazite grains gave an U-Pb age of 14.88 ± 0.35 Myr (Supplementary dataset 8b). These ages fall in the age range of regional (alkaline) volcanism (14 – 15 Ma; e.g. Prelević et al., 2008, 2012) and, more importantly, overlap with the age of the nearby syn-extensional 15.0 ± 0.3 Ma old Salihli granodiorite intrusion (Glodny & Hetzel, 2007).

The Hf isotopic composition of zircon domains with corresponding measured U-Pb age display a large range of $^{176}Hf/^{177}Hf_i$ values (Table 1; Supplementary dataset 11). The Miocene magmatic zircon grains from lamprophyre samples have $^{176}Hf/^{177}Hf_i$ values ranging from 0.282478 to 0.282531, with $\varepsilon Hf_{(15)}$ values varying between -8.6 to -10.5 (Figure 7a). Zircon xenocrysts show large variations in $\varepsilon Hf_{(15)}$ values, ranging from +5 to -50 (Figure 7a).

WHOLE-ROCK MAJOR AND TRACE ELEMENT GEOCHEMISTRY

Menderes lamprophyres (Table 2) plot in the field of basaltic andesite, basaltic trachyandesite, andesite, and trachyandesite in the total alkalis–silica (TAS) diagram (Figure 7b). A series of variation diagrams is presented in Figure 8 using MgO as a proxy for fractionation. Miocene Menderes granitoid rocks and basement metaigneous rocks of Cadomian age are also plotted for comparison. All lamprophyres form a continuous evolutionary trend with decreasing Fe_2O_3, TiO_2, Cr_2O_3 (not shown in the figure), and increasing SiO_2 towards more evolved MgO. The contents of Al_2O_3, CaO and alkali elements vary only a little with MgO content, although evolved samples seem to have a broader range of CaO and K_2O contents whereas more primitive lamprophyre samples show variable Na_2O contents. The lamprophyres, augen gneiss xenolith and Cadomian metaigneous rocks from the basement define continuous Harker trends with the low MgO concentrations of the most evolved lamprophyre samples overlapping with those of the least evolved Miocene granitic samples (Figure 8). The individual sills show considerable compositional variation. For example, SiO_2, MgO, and Mg# of Sill 7, which is only 4 m thick, vary from 52.6 to 58.4 wt%, 3.6 to 6 wt% and 0.58 to 0.66 wt%, respectively.

Trace element concentrations and ratios in the lamprophyres (Table 2) are mostly constant over the entire MgO range (Figures 9 and 10), except for Ba, Rb, Sr, and Th that show a relatively large spread. The trace element composition of most samples forms a continuous array projecting towards the compositional field of the Miocene Menderes granitoids. Exceptions to this correlation are the concentrations of La, which are highly variable in the Menderes granitoids, and Nb, for which the lamprophyres are slightly more enriched.

The enriched character of the lamprophyres is highlighted in a Primitive Mantle-normalised trace element abundance diagram (Figure 11a). All samples show a distinct positive Pb anomaly, as well as troughs for Nb, Ta, and Ti. Some samples have a positive Sr anomaly. Except for some scatter in Sr and the large-ion lithophile elements, the spidergram pattern for all lamprophyres are similar and resemble those of subduction zone magmas (e.g. Santorini, Figure 11a). In contrast, the various xenoliths show more variation and overall lower trace element contents, with peaks for Pb and troughs for Nb, Ta, and Ti typical of crustal rocks. The metasedimentary xenoliths (metapsammite, country rock, quartzite) have higher Zr and Hf contents than the lamprophyres. They also show troughs for Sr, most notably the quartzite xenolith. Calc-silicate and gneiss xenoliths have positive Sr peaks, whereas the augen gneiss xenolith has high K and U contents. An REE-spidergram (Figure 11b) illustrates that the lamprophyres have higher trace element contents than the various xenoliths and show enrichment in LREE over HREE and a subtle negative Eu anomaly.

WHOLE-ROCK RADIOGENIC ISOTOPES

The results of whole-rock radiogenic isotope analysis are presented in Table 3 and plotted in the standard Sr, Nd and Pb isotopic diagrams (Figure 12). Ratios used in the text and plots are age-corrected, i.e., are initial ratios for the time of emplacement of the lamprophyre sills. The emplacement age was also used to correct the xenolith data to obtain their isotopic composition at the time of assimilation. For comparison, Figure 12 also shows data for other Western Anatolian ultrapotassic volcanic rocks, the Miocene lamprophyres from Kos Island, the youngest Turkish volcanic rocks from Kula (only Sr-Nd) as well as the basement metaigneous rocks (mostly Cadomian age) and the Miocene Menderes granitoids.

The lamprophyres show a narrow range of Nd isotopic compositions ($^{143}Nd/^{144}Nd = 0.51247 – 0.51256$) and a large variation in Sr isotopic compositions ($^{87}Sr/^{86}Sr = 0.70609 – 0.71076$) (Figure 12a). Sr isotopic compositions can vary significantly among samples from the same sill. For instance, Sill 3 shows almost the entire observed compositional range (Figure 12a). Leaching the

lamprophyre powders with acetic acid produced leachates with more radiogenic Sr isotopic compositions than unleached powders (Figure 12a). The difference between $^{87}Sr/^{86}Sr_{leachate}$ and $^{87}Sr/^{86}Sr_{unleached}$ correlates well with the loss on ignition (LOI) of the whole rock powder (greater difference between leachate and unleached at higher LOI). The xenolithic material other than the augen gneiss, has less radiogenic Nd and similar or slightly more radiogenic Sr isotopic compositions than the hosting lamprophyres. The augen gneiss xenolith has a Sr and Nd isotopic signature almost identical to that of Miocene Menderes granites.

Plots of the Pb isotopic composition (Figures 12b and 12c) reveal a comparable variation to that shown by the Sr isotopes over the entire dataset. However, in contrast to Sr isotopes, the xenoliths overlap with Pb isotopic values of the lamprophyres and there is almost no variation in Pb isotopic composition between samples from one sill. In general, all samples follow the trend of Western Anatolian ultrapotassic volcanic rocks, which is almost parallel to the Northern Hemisphere Reference Line (NHRL; Hart, 1984) but at higher $^{207}Pb/^{204}Pb$ and higher $^{208}Pb/^{204}Pb$ for a given $^{206}Pb/^{204}Pb$.

GEO(THERMO)BAROMETRY

There is a wide range of published clinopyroxene- and amphibole-based thermobarometers (Hammarstrom & Zen, 1986; Johnson & Rutherford, 1989; Putirka, 2016; Ridolfi & Renzulli, 2012; Ridolfi *et al.*, 2010; Schmidt, 1992), and most of them are for silica-saturated rocks. The majority of amphibole-based thermobarometers rely on the presence of a restrictive multi-phase assemblage equilibrated with amphibole, which is not observed for the Menderes lamprophyres (e.g. titanite or/and magnetite). On the other hand, the inherent requirement of clinopyroxene models is to know the liquid composition in equilibrium with pyroxene, which greatly hinders their use in hybrid lavas like the Menderes lamprophyres. All these arguments narrow our choices to one recently developed amphibole-only geothermobarometers available (Ridolfi & Renzulli, 2012; Ridolfi *et al.* 2010; Ridolfi, 2020).

Table 4 presents the results of the amphibole-only geothermobarometer of Ridolfi & Renzulli (2012). Core and rim analyses were collected from amphibole grains with clear core and rim structures in BSE images (Supplementary dataset 7). For thermobarometry, we used the average compositions of cores and rims, respectively.

The calculated crystallization temperatures and pressures obtained for the studied amphiboles that demonstrate distinct petrographic and chemical zoning are considerably different between cores and rims (Ridolfi & Renzulli, 2012). The high Mg core zones have crystallization temperatures > 1020 °C and pressure above 7 kbar, whereas the low Mg rims have crystallization temperatures that are consistently below 1000 °C and pressures are lower than 4 kbar (Figure 13). We conclude that although the absolute values may be inaccurate, our geobarometric estimates imply that cores and rims of amphibole (and clinopyroxene) crystallised at considerably different depths.

DISCUSSION

The role of mantle-derived mafic melts in the genesis of silicic magmas during the formation of metamorphic core complexes is instrumental for the understanding of the evolution of the crust in extending terrains. Mafic magmatism may have a significant role in the generation of intermediate and silicic magmas, by triggering thermomechanical weakening, partial melting, mobilization of rheologically weakened parts of the solid crust and crustal flow. The generic model of the mantle-crust interaction builds upon the concept of underplating of the mafic magmas under the continental crust and include the following processes:

i Generation of mafic magmas by partial melting in the mantle,

ii Differentiation of mafic magma by crystallization within the crust or uppermost mantle;

iii The intracrustal evolution of mafic magma provides heat and volatiles (principally H_2O and CO_2) that will trigger crustal melting (Annen *et al.*, 2006a; Petford & Gallagher, 2001) and assimilation (DePaolo, 1981).

In a comprehensive view, the unique synergy of the above processes including the integration of multiple batches of variably differentiated mantle-derived melts and interaction with crustal material will be crucial to the development of a mantle-crust system.

GENERATION OF MENDERES LAMPROPHYRES

Lamprophyres: definition and origin

Lamprophyres encompass a variety of genetically different lava types that partially resemble several common magma groups, but are generated under more volatile-rich conditions. Therefore, lamprophyres are considered to represent merely a *facies* of common magmatic types and not a suite of comagmatic lavas (Mitchell, 1994). The calc-alkaline lamprophyres received their group name from the common association with calc-alkaline granitic rocks (Rock, 1977), and consist entirely of feldspar-bearing lamprophyres. This group includes phlogopite-dominated plagioclase-free minettes that demonstrate a close kinship with lamproites (Prelević *et al.*, 2004), and amphibole-dominated plagioclase-bearing kersantites (Le Maitre, 2002; Woolley *et al.*, 1996). Both of these calc-alkaline lamprophyre types show an alkaline character, and trace-element and isotopic enrichment, in conjunction with a broadly basaltic composition in terms of key major and compatible elements (Prelević *et al.*, 2004; Rock, 1977; Rock, 1983; Rock, 1991; Scarrow *et al.*, 2009; Tappe *et al.*, 2005). Altogether, these features indicate that the lamprophyres are near-primary melts derived from a heavily metasomatized mantle. Both lamprophyre types represent so-called orogenic potassic lavas with variably high K_2O contents (3–12 wt%), enrichment of K_2O relative to Na_2O, extreme trace element enrichment, and crust-like Sr, Nd, and Pb isotopic compositions (Foley & Peccerillo, 1992, Prelević *et al.*, 2008 and references therein). They are formed either by melting of subducted continent-derived sediments (Mallik *et al.*, 2016; Wang *et al.*, 2017) and the reaction of these melts with mantle peridotite in a single stage during subduction and collision (Campbell *et al.*, 2014) or by melting of phlogopite-rich pyroxenitic “metasomes”, so-called glimmerites, that had formed during an earlier (and possibly unrelated) tectonic event when K-rich

crust-derived fluids reacted with peridotite to form layers and veins (Conticelli *et al.*, 2013; Foley & Peccerillo, 1992; Förster *et al.*, 2020; Förster *et al.*, 2019a, b; Prelević *et al.*, 2013).

The close mutual proximity of the Menderes lamprophyric intrusions, their overall mineralogical similarity, and the coherent geochemical composition of different intrusive bodies suggest that the nine lamprophyre sills are comagmatic and genetically linked. Relatively high Mg# and compatible element abundances in the most primitive of the samples (> 5% MgO) imply that their parental magma is ultimately mantle-derived. They are potassium-rich, but with K_2O/Na_2O ratios below two (Figure 8h). Except for the unusually variable strontium isotopic signature that is interpreted to be directly related to carbonate xenoliths (Figure 12a; see also below), all other geochemical parameters including incompatible trace element pattern demonstrated by the Menderes lamprophyres are typical signatures of the orogenic mantle (Figure 11)(Prelević et al., 2008). Moreover, the Pb isotopic composition of the most mafic samples has values typical for the continental crust (Figure 12) especially with very radiogenic $^{207}Pb/^{204}Pb$, closely resembling the composition of some potassic and ultrapotassic lavas from the W. Anatolian Tertiary volcanic province (Akal, 2008; Akal *et al.*, 2013; Ersoy *et al.*, 2017; Prelević *et al.*, 2012, 2010, 2015). This resemblance implies that the Menderes lamprophyres are derived from a mantle source metasomatized by recycled continental crust, which is also typical for ultrapotassic lavas elsewhere along the Alpine-Himalayan belt (Prelević et al., 2008).

Menderes lamprophyres in a regional geochemical context

On the regional scale, Tertiary lavas from the West Anatolian Volcanic Province (WAVP) sampled the mantle beneath Western Anatolia and, therefore, represent a proxy for the various mantle sources that were accessible for melting during the formation of the Menderes lamprophyres. To a variable extent, rocks of the WAVP involved geochemical components derived from the convecting mantle (asthenosphere) and the lithospheric mantle (Figure 12). Based on Sr, Nd, and Pb isotope data two types of asthenosphere-derived 'anorogenic' components can be

distinguished. Component 1 (Figure 12) is characterised by unradiogenic $^{87}Sr/^{86}Sr$, and radiogenic $^{143}Nd/^{144}Nd$ and $^{206}Pb/^{204}Pb$. It is compositionally similar to the FOZO (FOcal ZOne) or HIMU (high-μ) components recognized in OIB (Hart et al., 1992; Stracke et al., 2005). This component is the most prominent one in some lamproitic and shoshonitic lavas from the southern parts of the WAVP and the Soke basin (Aldanmaz *et al.*, 2019; Prelević *et al.*, 2012, 2015). Component 2 (Figure 12) is chemically similar to the first one but has unradiogenic $^{206}Pb/^{204}Pb$ plotting closer to the field of the depleted mantle (DM; Zindler & Hart, 1986). This component is most pronounced in the lamprophyric lavas from Kos Island (Soder *et al.*, 2016) and Quaternary basanitic lavas at Kula (Alıcı *et al.*, 2002). In addition to the two asthenospheric components, there is a metasomatised lithospheric-mantle component (Component 3 in Figure 12) whose geochemical character of crust-like incompatible trace elements, radiogenic $^{87}Sr/^{86}Sr$ and $^{207}Pb/^{204}Pb$, and unradiogenic $^{143}Nd/^{144}Nd$ is ultimately derived from subducted continental crustal material (Prelević et al., 2012). This component, which may be stored in phlogopite–pyroxene-rich metasomes within the lithospheric mantle (Prelević et al., 2012) formed during earlier subduction episodes when subducted sediments produced high-Si melts (Förster *et al.*, 2019a, 2019b, 2018; Sekine & Wyllie, 1982) that interacted with the overlying mantle peridotite within the mantle wedge (Prelević et al., 2013). Intermediate compositions found in many lavas from the WAVP are most likely a result of mixing of magmas derived from these distinct components during partial melting of the mantle.

Additionally, two general spatial and temporal trends have been recognized in the composition of the Oligocene-Miocene mantle-derived magmatism across W. Anatolia. The first trend is a north-south directed age progression, which is coupled with a chemical change that indicates a dominance of the continental crust-derived metasomatic component (lithospheric mantle, Component 3 in Figure 12b) in the north and a southwardly increasing involvement of the asthenosphere-derived 'anorogenic' component (Component 1 in Figure 12b) (Francalanci *et al.*, 2000; Prelević *et al.*, 2012). The second trend is a west-east increase of incompatible trace element concentrations in comparably primitive Tertiary lavas indicating a decreasing influence of the second, DM-flavoured

asthenosphere-derived component (Component 2 in Figure 12b) on the geochemical composition of magmas; this trend correlates with the thickness of the lithospheric mantle beneath W Anatolia that increases in this direction. The eastward thickening of the metasomatized lithosphere may have allowed more extensive multi-stage melting and melt percolation processes probably causing this geochemical trend (Ersoy *et al.*, 2012).

The similar geochemical character of the Menderes lamprophyres and nearby Tertiary K-rich lavas from W. Anatolia implies that primary melts dominantly tapped the same lithospheric mantle source. More specifically, the isotopic composition of the Menderes lamprophyres demonstrates resemblance with the lamprophyres from Kos, the volcanism most-proximal to the Menderes lamprophyres. Available age data suggest that the Kos lamprophyric volcanism is of Miocene age (Soder *et al.*, 2016) predating the ongoing oceanic subduction in the active South Aegean Volcanic Arc (SAVA) (Bachmann *et al.*, 2019) formed during slab retreat due to post-orogenic back-arc extension (Jolivet & Brun, 2010; Meulenkamp *et al.*, 1988). The mixing of two enriched mantle components has been recognized in the Kos lamprophyres: a component geochemically resembling the subducted continent-derived sediments represented by low-Nb mica-lamprophyres (minettes), and incipient melts from the asthenosphere below the subducting slab represented by high-Nb amphibole-lamprophyres (kersantites) (Soder *et al.*, 2016). Hence, the orogenic signal must be due to a subduction-related metasomatic change in mantle compositions. Figure 12 demonstrates that the Menderes lavas plot as an extension of the Kos mica-lamprophyres.

In summary, several mantle geochemical components can be fingerprinted in the composition of the most primitive samples of Menderes lamprophyres. Their final composition represents a net effect of instantaneous mantle mixing with isotopic ratios and trace elements behaving in a regionally coherent fashion during post-orogenic mantle dynamics due to crust-mantle interaction in an active back-arc setting.

DIFFERENTIATION OF THE LAMPROPHYRE MAGMA WITHIN THE MENDERES CRUST

Very little attention has been paid to the role of magma evolution and to the extent such processes could affect the geochemical composition of calk-alkaline lamprophyres (Rock, 1991). One of the main reasons for this is that early studies of such rocks aimed to explain their extremely enriched geochemical character. It was realized that the concentrations of Sr, Nd and especially Pb in lamprophyres were usually more than twice those of typical continental crust (cf. crustal xenoliths in our samples, Figure 11). Due to this enriched character, the isotopic compositions of lamprophyric/lamproitic magmas are not sensitive to minor or moderate crustal contamination. Consequently, we may consider that the enriched signature of lamprophyres reflects their crustally-contaminated mantle source (Conticelli, 1998). However, for the same reason, namely the extreme enrichment of their parental melts, potentially significant crustal contamination of these magmas may be obscured. Even considerable melt contamination may result only in slight "dilution" of parameters sensitive for contamination processes. The originally high content of "typically crustal" elements in lamprophyres that is a primary feature derived from their mantle source, systematically compensate chemical changes that originate due to low-P contamination processes by continental crustal lithologies, which have considerably lower concentrations in the relevant elements.

Identification of evolutional processes

There are several lines of evidence demonstrating that the proto-lamprophyric magma was contaminated by mixing and/or crustal assimilation deep in the crust, and that the compositional variation of the Menderes lamprophyres (Figure 8 and 9) is not due to fractional crystallization alone:

- The observed variation in the isotopic composition of Sr and Nd (Figure 12) precludes simple fractional crystallization as the sole process of lamprophyre evolution; putting that in a regional crustal dynamic context, the convergence from the most mafic end-members

towards the data of the coeval Salihli and Turgutlu granites (Figures 8, 9, and 10) implies a genetic and, probably, a mixing relationship.

- The lamprophyres carry a "crystal and rock cargo" including zircon xenocrysts and quartz and carbonate ocelli, as well as partially molten xenolithic material derived from the basement lithologies, all of which represent truly foreign material. The U-Pb ages of numerous zircon xenocrysts, as well as augen gneiss xenoliths, demonstrate that they are derived from the Cadomian basement from the core series (Supplementary dataset 8a) and not from the immediate place of intrusion that encompasses metasedimentary rocks from the cover series. On the other hand, quartz and carbonate ocelli are derived from the wall rocks and are in chemical disequilibrium with the host magma as demonstrated by the reaction rims (Figure 3f). Therefore, the magma contains minerals and rocks from several sources, which implies that assimilation played an important role during its intracrustal evolution.
- Clinopyroxene and amphibole xenocrysts are zoned with abrupt compositional changes at the contact between the internally homogenous cores and rims (Figure 4). The change in major element composition is also reflected in variations of trace element contents (Figure 5 and 6). Neither fractional crystallisation nor diffusion can explain the observed sharp patterns. Simple fractional crystallisation would lead to a more continuous and broadly linear decrease of many minor and trace element abundances (e.g., Ti, Zr, Sr, Ba, Eu, Hf) that correlate with Mg#. Slowly diffusing elements such as Ti, Zr and REE and fast diffusing elements like Sr, Na, Rb show similar zoning, which implies that their distribution is coupled and, therefore is not controlled by diffusion. Thus, the contrasting composition of cores and rims implies that the cores record crystallization from a proto-lamprophyre magma and the rims record crystallization after the magma composition was changed by assimilation or magma mixing.

The above arguments seem to partly contradict the results of simple modelling of magma-mixing vs. assimilation-plus-fractional-crystallisation (AFC) processes (Supplementary dataset 12),

which suggest that the AFC model (DePaolo, 1981) with fractionation-dominated differentiation explains the geochemical variation shown by the Menderes lamprophyres better than a magma mixing scenario. However, without a doubt this approach is model dependent, as we cannot pinpoint the potential contaminant with any certainty.

In summary, the chemical variation observed in the Menderes lamprophyres can be narrowed down to two processes which are indisputable, mutually inclusive and equally viable: i) magma mixing and mingling between a primary mantle-derived proto-lamprophyric melt and a granitic crustal-bearing mush compositionally similar to the nearby coeval Salihli and Turgutly granites, and/or ii) fractional crystallization combined with assimilation (AFC) of country rock and/or lithologies the magma encountered during ascent, including the (metagranitic) augen gneiss.

Constraints from zircon compositions and the age

The prevalence of Cadomian ages with predominantly sub-chondritic □Hf values amongst zircon xenocrysts (Supplementary dataset 8 and Figure 7a) allows us to infer that the source of these zircon grains needs to be S-type granitic material (Avigad et al., 2016) supporting the notion that the augen gneiss may represent the main contaminant of the proto-lamprophyric melt (Figure 7a). Newly formed zircon grains have variable and unradiogenic Hf-isotopic signature (Figure 10a), which is even more unradiogenic than the most unradiogenic Hf signature demonstrated by Tertiary alkaline lavas from Western Anatolia (Prelević et al., 2010). Their relatively large range of Hf-isotopic signatures indicates that young zircon grains crystallized from different parts of the magmatic system (a series of melt pockets, conduits and magma chambers), ranging from variably contaminated mafic melts to local crustal melt. The chemical heterogeneity of young (magmatic) zircon population provides direct evidence for melt-crust interaction in a dynamic system with periods of zircon undersaturation and regrowth during transfer between different melt batches. Importantly, this implies that the contamination with the crust was not only restricted to melt pockets and small chambers during emplacement of the lamprophyric melt but represents a feature of the entire crustal magmatic history of the lamprophyre magma.

Constraints from thermobarometric limitations and mineral compositions

Amphibole grains from the Menderes lamprophyres comprise plateau-like core compositions with Mg# up to 76, and relatively high Al_2O_3 up to 13 % (Figure 4), surrounded by invariably lower Mg# and Al_2O_3. The prominent plateau-like core domains formed at an early stage, crystallising at ca 1020 – 1060 ^{o}C and a depth between 30-35 km (Figure 13). These cores also recorded large variations in some petrogenetically-relevant trace element ratios (e.g. Dy/Yb, see Figures 5, 6) at invariable and high Mg#. Similar trace element variation has been recorded in clinopyroxene cores (Figures 5, 6). The ratios of similarly incompatible trace elements cannot be changed by crystal fractionation, which especially applies to the REE that show similar geochemical behaviour. Crystal chemistry of clinopyroxene (in particular their Ca-Tschermakite-component) may influence the partition coefficient of REEs (e.g. Gaetani & Grove, 1995). Because of the very low CaTs-components in clinopyroxene and comparable trace element behaviour in amphiboles, this effect may not have been significant for the Menderes lamprophyres. Instead, the broad range of REE fractionation among cores of different clinopyroxene and amphibole crystals having comparable Mg# and absolute REE concentrations cannot be due to fractional crystallisation and/or assimilation of crustal material (Figure 5, 6). Hence, different clinopyroxene and amphibole cores must have formed from primary magmas of different compositions. Such variations also may account for the subtle but significant variation of Nd isotopes in most mafic samples, especially the ones showing an increase in $^{143}Nd/^{144}Nd$ with a decrease of MgO and/or compatible elements (Supplementary dataset 11).

Amphibole cores are embayed and rimmed by green hornblende that crystallized at < 980 ^{o}C. Most trace elements (Zr, Hf, Sr, Ti, V, REE) demonstrate a sudden increase relative to the cores, which is consistent with crystallisation from a compositionally more evolved and homogenous magma. Similarly, clinopyroxene rims have different compositions from the cores, supporting crystallisation from a more evolved melt. Several arguments support that notion:

i The increase of REE contents and a constant and ubiquitous Eu-anomaly in the rims of amphibole and clinopyroxene (Figure 5, 6) reflects the evolved character of the melt from which amphibole and clinopyroxene rims crystallised. Alternatively, the simultaneous fractional crystallization of plagioclase would have a similar effect, but it does not agree with observations, as plagioclase is not a phenocrystic phase (it is universally restricted to the groundmass).

ii Rb and Ba are decoupled, with Rb decreasing and Ba increasing in the amphibole rim (Figure 5, 6). This implies that the melt mixing with the proto-lamprophyre magmas must have high Ba and low Rb contents, as these large-ion lithophile elements are incompatible in amphibole (Nandedkar *et al.*, 2016). Co-precipitation of phlogopite with amphibole, which has been observed texturally in some samples, would decrease both Ba and Rb contents in amphiboles due to an increase of the bulk partition coefficient. Moreover, increased Ti contents at decreasing MgO (Figure 4) are inconsistent with mere coeval fractionation of hornblende and biotite, as Ti contents should be decreasing.

iii Different, but internally constant, Zr concentrations between cores and rims indicate that hornblende and zircon didn't crystallize together, suggesting that zircon saturation had not been reached when the phenocrysts formed.

In conclusion, the most likely mechanism for the generation of the amphibole and clinopyroxene rims is by mixing and homogenisation with a felsic melt, depleted in Eu and with higher Ba and lower Rb contents than the parental, "proto-lamprophyric" melts from which the variable phenocrystic cores crystallised.

Carbonate assimilation drives the Sr isotopic variability

The variation in whole-rock $^{87}Sr/^{86}Sr$ in Menderes lamprophyres (Figure 12a) shows that process additional to AFC and magma mixing/mingling must have acted. The decoupling of Sr and Nd isotopes and the sub-horizontal variation in $^{87}Sr/^{86}Sr$ among different and within individual samples indicate selective addition of radiogenic Sr. Menderes lamprophyres have variable, but

usually very high loss on ignition (LOI) of up to 10 wt%. LOI is the only geochemical parameter that correlates with $^{87}Sr/^{86}Sr$. Therefore, we leached an aliquot of powders of all samples measured for $^{87}Sr/^{86}Sr$ with weak acetic acid and measured the leachate. Our data show that the leachate in all samples has considerably higher $^{87}Sr/^{86}Sr$ than the corresponding unleached samples, and the difference between leachate and the unleached sample is greater for samples with higher LOI. Therefore, we ascribe the high $^{87}Sr/^{86}Sr$ signal of the lamprophyres to carbonate minerals because (a) the lamprophyres have abundant carbonate ocelli, which are significantly larger than any other phenocryst, show reaction rims (see Figure 3e) and, therefore, are interpreted as xenocrysts; (b) the carbonate ocellis have high Sr contents (up to 2000 ppm SrO_2) and, hence, contribute significantly to the Sr budget of the rocks; (c) different amounts of incorporated carbonates explain the observed within-sill variation in Sr isotopic composition; and (d) carbonates dominate the CO_2 budget of the rock and contribute significantly to the Sr budget, which explains the correlation of $^{87}Sr/^{86}Sr$ with LOI.

Clinopyroxene crystals in a reaction zone around carbonate xenocrysts can have high Mg# comparable to Group I clinopyroxene cores but have lower Cr_2O_3 contents. Hence, the carbonates were probably incorporated during ascent, before Group I rim formation (as the ocelli pyroxenes still have high Mg#), but after Group I core formation (as they have lower Cr_2O_3). In contrast, the overall evolved character of clinopyroxene around quartz resembles Group II clinopyroxene rim compositions implying very late assimilation of quartz, probably at the depth of final emplacement (into quartz-rich metapsammites).

INTRACRUSTAL MAGMAGENESIS AND THE ORIGIN OF THE MENDERES METAMORPHIC CORE COMPLEX

Lamprophyres and granites: a genetic relationship

Global spatial and temporal association of lamprophyres with nearby granitoid bodies led to the proposition of a genetic link of lamprophyres with more evolved plutonic rocks (e.g. Fowler & Henney, 1996; Prelević *et al.*, 2004; Rock, 1991; Sheppard, 1995). Probably the most speculative notion is that calk-alkaline lamprophyres indeed represent parental melts to many granitoid plutons (Rock, 1991). A more viable model, which can be applied to lamprophyres and associated syn-extensional granites in the Menderes metamorphic core complex, proposes that hybridization of a volatile-laden alkaline proto-lamprophyric melt with felsic magma represents a main driving force for the production of several types of intermediate compositions (Prelević *et al.*, 2004). The close and genetic relationship between the lamprophyres and granites in the Menderes metamorphic core complex may be a reflection of the following: the heavily metasomatized lithospheric mantle that has been activated by slab roll-back and/or a slab window and created volatile-laden melts (Ersoy & Palmer, 2013; Prelević *et al.*, 2012, 2015; Soder *et al.*, 2016), which in turn facilitate the melting of the crust composed of juvenile magmatic material, namely the lower crust of the Menderes region that is dominated by augen gneiss.

The high volatile contents of proto-lamprophyric magmas represent the most important parameter of these small-volume melts to contribute to crustal melting. The release of water from lamprophyric magmas will trigger fluid-present crustal melting (Brown *et al.*, 2008), whereas the release of CO_2 would destabilize hydrous phases in the lower crust inducing anhydrous melting (Cuney & Barbey, 2014). Also, lamprophyric/lamproitic melts are typically enriched in F and Cl (Foley, 1989a, 1989b, 1990, Prelević *et al.*, 2004), which are important agents in deep-crustal metamorphism and anatexis (Cuney & Barbey, 2014). In the lower crust these agents in combination with latent heat and liberated H_2O, may contribute to granite production, leading to larger melt fractions than for simple dehydration melting. The strong morphological and chemical core-rim zonation of clinopyroxene and amphibole phenocrysts observed in Menderes lamprophyres resulted after hybridisation with the partially molten crustal material. The prolonged crystallization of amphibole and mica even after the change in magma composition implies that the

hybrid magmas were still highly charged with volatiles, having a chance to continuously contribute to further crustal melting. All these arguments highlight the importance of hydrous mantle-crust interaction in the origin of core complexes, even in cases when voluminous surface magmatism is lacking.

Linking granite generation to specific crustal lithologies requires knowledge of the protolith composition. We infer that the majority of Cenozoic W. Anatolian granitic plutons are, at least partially, a product of crustal melting triggered by mafic magmas (Annen *et al.*, 2006a, b). Figure 14 plots Nd isotopic composition of the Menderes granitic intrusions versus age. The plot demonstrates a considerable drop of the □Nd value of magmatic rocks from the outer parts of the Menderes Massif to rocks from the centre of the massif, resembling the isotopic composition of the Cadomian basement including the augen gneisses. This is also apparent from the distribution of ages obtained on zircon xenocrysts (Supplementary dataset 8). The □Nd and the zircon age distribution imply that Cadomian basement rocks dominated by the augen gneisses are likely protoliths of the Menderes granites. The isotopic signature of granitic plutons outside the Menderes metamorphic core complex is more radiogenic, where Upper Palaeozoic and Mesozoic sequences make up the basement (Avigad *et al.*, 2016). We infer that the specific geochemical properties that characterize magmatism of the central Menderes Massif, that is the input of hydrous basaltic magmas, enhanced by interaction with the fertile crust dominantly composed of augen gneiss, increased the intensity of the anatexis and ultimately triggered core complex building.

Mantle-crust interaction in the Menderes metamorphic core complex: a working model

Figure 15 illustrates the structure of the Menderes crust and pathways of melt evolution beneath the Menderes metamorphic core complex. The preferred evolutional model for lamprophyric melt at crustal levels is in line with the complete dataset.

1. The first batches of proto-lamprophyre melt were generated and ascended to a deep crustal level, where they were stored in a single or several magma chambers. The trace element

compositions of early (high Mg cores) amphibole, phlogopite and clinopyroxene phenocrysts reflect the composition of the primary melt. This stage of magma evolution is preserved in the high Dy/Yb cores of amphibole and clinopyroxene. Subsequent melt batches of different compositions (variable Dy/Yb) were mixed into the magma chamber(s), changing the (trace element) composition of the magma. This primary magma compositional variation is recorded in the continuous range from high Dy/Yb to lower Dy/Yb observed in the cores of zoned amphibole and Group I clinopyroxene (Figure 5, 6). The chemical variability of these proto-lamprophyric melt batches is also recorded by Nd isotopes (Supplementary dataset 11). It reflects the heterogeneity of the lamprophyric mantle source, geochemically also observed in the source of the Kos island lamprophyres (Soder *et al.*, 2016).

2. Crystallization of the volatile-rich lamprophyre magma released fluids that triggered the melting of the Cadomian lower crust. This melting event produced a melt with Si-rich composition similar to the Salihli and Turgutlu granites, together with a crystal cargo dominated by unmelted zircon crystals of Cadomian and older age and partially-molten augen gneiss fragments. For the lamprophyres, mixing with these felsic crustal melts results in a distinct change in the chemical and isotopic composition of the melt. Mixing is most prominently recorded by the chemical zonations of clinopyroxene and amphibole, and ultimately, these crustal melt portions have a large chance to contribute or even represent magmatic pulses that intruded as Salihli and Turgutlu granitic intrusions. The sudden jump in composition between the cores and rims of the lamprophyric phenocrysts is a result of a (rapid) change in magma composition. Therefore, during ascent from the lower crustal storage to the level of final emplacement, the magma must have been hybridized by mixing with a low-Mg, most likely felsic melt. The composition of the phenocryst rims indicates that this melt had an Eu anomaly and was enriched in incompatible trace elements. The uniform trace element ratios in the rims, which are similar to the low Dy/Yb end of the spread displayed by cores, suggest that no new mantle melt-batches were mixed into the hybrid magma. During the ascent and emplacement of the hybrid magma, crustal lithologies were incorporated. These

xenoliths were not assimilated to a significant extent. The different xenoliths in the lamprophyres represent lithologies common in the Menderes crust.

3. Assimilation of carbonates, most probably representing marble intercalations in graphite-bearing phyllites sampled during ascent, represents the last modification of the chemical composition of the lamprophyres.

The intrusion of the lamprophyres at 15 Ma happened contemporaneously to the main stage of exhumation of the central Menderes metamorphic core complex as established by the development of horst-graben systems in the Early Miocene (Yılmaz et al., 2000) and the intrusion of the nearby extensional Salihli and Turgutlu granitic intrusions (Catlos *et al.*, 2010, Glodny & Hetzel, 2007). Recent thermochronology data (Buscher *et al.*, 2013; Nilius *et al.*, 2019) indicate that exhumation in the central part occurred at high exhumation rates and predominantly by tectonic denudation, whereas rocks at the southern flank were mainly exhumed by erosion. Available data suggest that the central part of the Menderes metamorphic core complex exhumed very quickly, which is in line with the presence of clasts of high-grade metamorphic rocks derived from the core series in Miocene sediments of the Gediz Graben, demonstrating that portions of the core series of the Menderes metamorphic core complex were exhumed to the surface already in the early Miocene (Çemen *et al.*, 2006, Ciftci & Bozkurt, 2009). This fact further supports the notion that the exhumation of the core of the Menderes has been triggered and facilitated by a synergy of the above two coinciding processes: magmatism and extension.

ACKNOWLEDGEMENTS

This work was supported through the Inneruniversitäre Forschungsförderung, University of Mainz, and Serbian Ministry of Education, Science and Technological Development, Grant/Award Number: 176016. We would like to thank B. Hübner and H. Rothe (both GFZ) for help with sample leaching and ion-exchange chromatography. Stephan Buhre and Nora Groschopf of the Mainz University, are thanked for assistance with the microprobe. We are very grateful to three anonymous

reviewers for reading one of the earlier versions of the manuscript, and the editor for handling our manuscript. This is FIERCE contribution No. 96.

References

Agostini, S., Doglioni, C., Innocenti, F., Piero, M., Tonarini, S. & Savaşçın, M. (2007). The transition from subduction-related to intraplate Neogene magmatism in the Western Anatolia and Aegean area. 1-15.

Akal, C. (1993). Occurrence, emplacement and origin of granites in the Northern part of Odemis (Kiraz Submassif), Western Turkey. *Graduate School of Natural and Applied Sciences*. Izmir, Turkey: T.C. Dokuz Eylul University, .

Akal, C. (2008). K-Richterite-Olivine -Phlogopite-Diopside-Sanidine Lamproites From The Afyon Volcanic Province, Turkey. *Geological Magazine* **145**, 1–16.

Akal, C., Helvaci, C., Prelević, D. & van den Bogaard, P. (2013). High-K volcanism in the Afyon region, western Turkey: from Si-oversaturated to Si-undersaturated volcanism. *International Journal of Earth Sciences* **102**, 435-453.

Aldanmaz, E., Pearce, J. A., Thirlwall, M. F. & Mitchell, J. G. (2000). Petrogenetic evolution of late Cenozoic, post-collision volcanism in western Anatolia, Turkey. *Journal of Volcanology and Geothermal Research* **102**, 67-95.

Aldanmaz, E., Altunkaynak, Ş. & Güçtekin, A. (2019). Some remarks on the nature of mantle metasomatism beneath western Anatolian–Aegean region: Contrasting isotopic signatures recorded in the Miocene lavas from the Söke Basin. *Geological Journal* **54**, 3860-3877.

Alıcı, P., Temel, A. & Gourgaud, A. (2002). Pb-Nd-Sr isotope and trace element geochemistry of Quaternary extension-related alkaline volcanism: a case study of Kula region (western Anatolia, Turkey). *Journal of Volcanology and Geothermal Research* **115**, 487-510.

Altunkaynak, S. & Dilek, Y. (2006). Timing and nature of Postcollisional volcanism in western Anatolia and geodynamic implications. In: Dilek, Y. & Pavlides, S. (eds.) *Postcollisional Tectonics and Magmatisam in the Mediterranean region and Asia*: The geological society of America, 321-353.

Amato, J. & Miller, E. (2004). Geologic map and summary of the evolution of the Kigluaik Mountains gneiss dome, Seward Peninsula, Alaska. *Gneiss Domes in Orogeny* **380**, 295-306.

Annen, C., Blundy, J. & Sparks, S. (2006a). The source of granitic melt in Deep Hot Zones. *Transactions of the Royal Society of Edinburgh: Earth Sciences* **97**, 297-309.

Annen, C., Blundy, J. D. & Sparks, R. S. J. (2006b). The Genesis of Intermediate and Silicic Magmas in Deep Crustal Hot Zones. *J. Petrology* **47**, 505-539.

Avigad, D., Abbo, A. & Gerdes, A. (2016). Origin of the Eastern Mediterranean: Neotethys rifting along a cryptic Cadomian suture with Afro-Arabia. *GSA Bulletin* **128**, 1286-1296.

Bachmann, O., Allen, S. & Bouvet de Maisonneuve, C. (2019). The Kos-Nisyros-Yali Volcanic Field. Elements **15**, 191-196.

Bailey, J. C. , Jensen E., Hansen A., Kann A., & Kann K. (2009), Formation of heterogeneous magmatic series beneath North Santorini, South Aegean island arc, Lithos, 110 (1), 20–36.

Biryol, B. C., Beck, S. L., Zandt, G. & Özacar, A. A. (2011). Segmented African lithosphere beneath the Anatolian region inferred from teleseismic P-wave tomography. *Geophysical Journal International* **184**, 1037-1057.

Bocchini, G. M., Brüstle, A., Becker, D., Meier, T., van Keken, P. E., Ruscic, M., Papadopoulos, G.A., Rische, M. & Friederich, W. (2018). Tearing, Segmentation, and Backstepping of Subduction in the Aegean: New Insights from Seismicity. Tectonophysics 734-735, 96–118.

Bozkurt, E. & Mittwede, S. K. (2001). Introduction to the Geology of Turkey-A Synthesis. *International Geology Review* **43**, 578-594.

Bozkurt, E. & Oberhänsli, R. (2001). Menderes Massif (Western Turkey): structural, metamorphic and magmatic evolution – a synthesis. *International Journal of Earth Sciences* **89**, 679-708.

Bozkurt, E., Winchester, J. A., Mittwede, S., & Ottley, C. (2006). Geochemistry and tectonic implications of leucogranites and tourmalines of the Southern Menderes Massif, Southwest Turkey. Geodinamica Acta, 19, 363–390.

Brown, P. E., Ryan, P. D., Soper, N. J. & Woodcock, N. H. (2008). The Newer Granite problem revisited: a transtensional origin for the Early Devonian Trans-Suture Suite. *Geological Magazine* **145**, 235-256.

Buscher, J., Hampel, A., Hetzel, R., Dunkl, I., Glotzbach, C., Struffert, A., Akal, C. & Rätz, M. (2013). Quantifying rates of detachment faulting and erosion in the central Menderes Massif (western Turkey) by thermochronology and cosmogenic 10Be. *Journal of the Geological Society* **170**, 1447.

Campbell, I. H., Stepanov, A. S., Liang, H.-Y., Allen, C. M., Norman, M. D., Zhang, Y.-Q. & Xie, Y.-W. (2014). The origin of shoshonites: new insights from the Tertiary high-potassium intrusions of eastern Tibet. *Contributions to Mineralogy and Petrology* **167**, 983.

Candan, O., Dora, O. Ö., Oberhänsli, R., Çetinkaplan, M., Partzsch, J. H., Warkus, F., & Dürr, S. (2001). Pan-African high-pressure metamorphism in the Precambrian basement of the Menderes Massif, Western Anatolia, Turkey. International Journal of Earth Sciences, 89, 793–811.

Candan, O., Dora, O. Ö., Oberhänsli, R., Koralay, O. E., Çetinkaplan, M., Akal, C., Satır, M., Chen, F., & Kaya, O. (2011). Stratigraphy of the Pan-African Basement of the Menderes Massif and the relationship with late Neoproterozoic/Cambrian evolution of the Gondwana. Bulletin of the Mineral Research and Exploration, 142, 25–69.Catlos, E. J., Baker, C., Sorensen, S. S., Çemen, I. & Hançer, M. (2010). Geochemistry, geochronology, and cathodoluminescence imagery of the Salihli and Turgutlu granites (central Menderes Massif, western Turkey): Implications for Aegean tectonics. *Tectonophysics* **488**, 110-130.

Çemen, I., Catlos, E. J., Gogus, O. & Ozerdem, C. (2006). Post-Collisional Extensional Tectonics and Exhumation of the Menderes Massif in the Western Anatolia Extended Terrane, Turkey. In: Dilek, Y. (ed.) *Postcollisional Tectonics and Magmatism in the Eastern Mediterranean Region*: Geological Society of America's Special Paper 353-379.

Ciftci, B. & Bozkurt, E. (2009). Structural evolution of the Gediz Graben, SW Turkey: Temporal and spatial variation of the graben basin. *Basin Research* **22**, 846-873.

Collins, A. S. & Robertson, A. H. F. (1999). Evolution of the Lycian Allochthon, western Turkey, as a north-facing Late Palaeozoic to Mesozoic rift and passive continental margin. *Geological Journal* **34**, 107-138.

Conticelli, S. (1998). The effect of crustal contamination on ultrapotassic magmas with lamproitic affinity: mineralogical, geochemical and isotope data from the Torre Alfina lavas and xenoliths, Central Italy. Chemical Geololgy 149, 51-81.

Conticelli, S., Avanzinelli, R., Poli, G., Braschi, E. & Giordano, G. (2013). Shift from lamproite-like to leucititic rocks: Sr-Nd-Pb isotope data from the Monte Cimino volcanic complex vs. the Vico stratovolcano, Central Italy. *Chemical Geology* **353**, 246-266.

Crittenden, M., Jr., Coney, P. J. & Davis, G. (1978). Tectonic significance of metamorphic core complexes in the North American Cordillera. *Geology* **6**, 79-80.

Cuney, M. & Barbey, P. (2014). Uranium, rare metals, and granulite-facies metamorphism. *Geoscience Frontiers* **5**, 729-745.

DePaolo, D. J. (1981). Trace element and isotopic effects of combined wallrock assimilation and fractional crystallization. *Earth and Planetary Science Letters* **53**, 189.

Dewey, J. F. & Şengör, A. M. C. L. (1979). Aegean and surrounding regions: Complex multiplate and continuum tectonics in a convergent zone. *GSA Bulletin* **90**, 84-92.

Doğru, F., Ankaya Pamukçu, O., Gönenç, T. & Yildiz, H. (2018). Lithospheric structure of western Anatolia and the Aegean Sea using GOCE-based gravity field model. *Bollettino di Geofisica Teorica ed Applicata* **59**, 135-160.

Dunkl, I., Mikes, T., Simon, K. & Eynatten, H. (2008). Brief introduction to the Windows program Pepita: data visualization, and reduction, Mineralogical Association of Canada, Short Course, **40**, 334-340.

Erdmann, S., Martel, C., Pichavant, M. & Kushnir, A. R. L. (2014). Amphibole as an archivist of magmatic crystallization conditions: Problems, potential, and implications for inferring magma storage prior to the paroxysmal 2010 eruption of Mount Merapi, Indonesia. *Contributions to Mineralogy and Petrology* **167**, 1016.

Erkül, F., Erkül, S. T., Ersoy, Y., Uysal, İ. & Klötzli, U. (2013). Petrology, mineral chemistry and Sr–Nd–Pb isotopic compositions of granitoids in the central Menderes metamorphic core complex: Constraints on the evolution of Aegean lithosphere slab. Lithos **180-181**, 74-91.

Erkül, S. T. (2012). Petrogenetic evolution of the Early Miocene Alaçamdağ volcano-plutonic complex, northwestern Turkey: implications for the geodynamic framework of the Aegean region. *International Journal of Earth Sciences* **101**, 197-219.

Erkül, S. T. & Erkül, F. (2012). Magma interaction processes in syn-extensional granitoids: The Tertiary Menderes Metamorphic Core Complex, western Turkey. *Lithos* **142-143**, 16-33.

Ersoy, Y. E., Helvaci, C. & Palmer, M. R. (2012). Petrogenesis of the Neogene volcanic units in the NE-SW-trending basins in western Anatolia, Turkey. Contributions to Mineralogy and Petrology **163**, 379-401.

Ersoy, E. Y. & Palmer, M. R. (2013). Eocene-Quaternary magmatic activity in the Aegean: Implications for mantle metasomatism and magma genesis in an evolving orogeny. *Lithos* **180-181**, 5-24.

Ersoy, E. Y., Palmer, M. R., Genç, Ş. C., Prelević, D., Akal, C. & Uysal, I. (2017). Chemo-probe into the mantle origin of the NW Anatolia Eocene to Miocene volcanic rocks: Implications for the role of, crustal accretion, subduction, slab roll-back and slab break-off processes in genesis of post-collisional magmatism. *Lithos* **288-289**, 55-71.

Ersoy, Y. & Helvaci, C. (2007). Stratigraphy and geochemical features of the early miocene bimodal (ultrapotassic and calc-alkaline) volcanic activity within the NE-trending Selendi Basin, western Anatolia, Turkey. *Turkish Journal of Earth Sciences* **16**, 117-139.

Ersoy, Y., Helvaci, C., Sozbilir, H., Erkul, F. & Bozkurt, E. (2008). A geochemical approach to Neogene-Quaternary volcanic activity of western Anatolia: An example of episodic bimodal volcanism within the Selendi Basin, Turkey. *Chemical Geology* **255**, 265-282.

Fischer, S., Prelević , D. & Akal, C. (2010). Alkaline intrusives and what they tell us about the uplift of the Menderes Massif, W. Anatolia, Turkey. In: Dilek, Y. & Bozkurt, E. (eds.) *Tectonic Crossroads: Evolving Orogens of Eurasia-Africa-Arabia*. Ankara, Turkey: The Geological Society of America, 21-19 BTH 22 [175479].

Foley, S. & Peccerillo, A. (1992). Potassic and ultrapotassic magmas and their origin. *Lithos* **28**, 181.

Foley, S. F. (1989a). Experimental constraints of phlogopite chemistry in lamproites; 1, The effect of water activity and oxygen fugacity. *European Journal of Mineralogy* **1**, 411-426.

Foley, S. F. (1989b). The genesis of lamproitic magmas in a reduced fluorine-rich mantle. In: Ross, J., Jacques, A. L., Ferguson, J., Green, D. H., O'Reilly, S. Y., Danchin, R. V. & Janse, A. J. A. (eds.) *Fourth International Kimberlite Conference*. Perth, Australia: Geological Society of Australia, 616–631.

Foley, S. F. (1990). A review and assessment of experiments on kimberlites, lamproites and lamprophyres as a guide to their origin. *Special issue on Experimental petrology*. Bangalore, India: Indian Academy of Sciences, 57-80.

Förster, M. W., Buhre, S., Xu, B., Prelević, D., Mertz-Kraus, R. & Foley, S. F. (2020). Two-Stage Origin of K-Enrichment in Ultrapotassic Magmatism Simulated by Melting of Experimentally Metasomatized Mantle. *Minerals* **10**, 41.

Förster, M. W., Prelević, D., Buhre, S., Mertz-Kraus, R. & Foley, S. F. (2019a). An experimental study of the role of partial melts of sediments versus mantle melts in the sources of potassic magmatism. *Journal of Asian Earth Sciences* **177**, 76-88.

Förster, M. W., Buhre, S., Xu, B., Prelević, D., Mertz-Kraus, R. & Foley, S. F. (2019b). Two-Stage Origin of K-Enrichment in Ultrapotassic Magmatism Simulated by Melting of Experimentally Metasomatized Mantle. *Minerals* **10**, 41.

Förster, M. W., Prelević, D., Buhre, S., Mertz-Kraus, R. & Foley, S. F. (2019b). An experimental study of the role of partial melts of sediments versus mantle melts in the sources of potassic magmatism. *Journal of Asian Earth Sciences* **177**, 76-88.

Förster, M. W., Prelević, D., Schmück, H. R., Buhre, S., Marschall, H. R., Mertz-Kraus, R. & Jacob, D. E. (2018). Melting phlogopite-rich MARID: Lamproites and the role of alkalis in olivine-liquid Ni-partitioning. *Chemical Geology* **476**, 429-440.

Fowler, M. B. & Henney, P. J. (1996). Mixed Caledonian appinite magmas: implications for lamprophyre fractionation and high Ba-Sr granite genesis. *Contributions to Mineralogy and Petrology* **126**, 199-215.

Francalanci, L., Innocenti, F., Manetti, P. & Savascin, M. Y. (2000). Neogene alkaline volcanism of the Afyon-Isparta area, Turkey: petrogenesis and geodynamic implications. *Mineralogy and Petrology* **70**, 285-312.

Gaetani, G. A. & Grove, T. L. (1995). Partitioning of rare earth elements between clinopyroxene and silicate melt: Crystal-chemical controls Geochimica et Cosmochimica Acta **59**, 1951-1962.

Gerdes, A. & Zeh, A. (2006). Combined U-Pb and Hf isotope LA-(MC-)ICP-MS analyses of detrital zircons: Comparison with SHRIMP and new constraints for the provenance and age of an Armorican metasediment in Central Germany. *Earth and Planetary Science Letters* **249**, 47-61.

Gessner, K., Gallardo, L. A., Markwitz, V., Ring, U. & Thomson, S. N. (2013). What caused the denudation of the Menderes Massif: Review of crustal evolution, lithosphere structure, and dynamic topography in southwest Turkey. *Gondwana Research* **24**, 243-274.

Glodny, J. & Hetzel, R. (2007). Precise U-Pb ages of syn-extensional Miocene intrusions in the central Menderes Massif, western Turkey. *Geological Magazine* **144**, 235-246.

Gürsu, S. (2016). A new petrogenetic model for meta-granitic rocks in the central and southern Menderes Massif – W. Turkey: Implicationsfor Cadomian crustal evolution within the Pan-African mega-cycle. Precambrian Research, 275, 450–470.

Hart, S. R., Hauri, E. H., Oschmann, L. A. & Whitehead, J. A. (1992). Mantle plumes and entrainment; isotopic evidence. Science **256**, 517-520.

Hammarstrom, J. M. & Zen, E. (1986). Aluminium in hornblende; an empirical igneous geobarometer. *American Mineralogist* **71**, 1297-1313.

Hasozbek, A., Akay, E., Erdogan, B., Satir, M. & Siebel, W. (2010). Early Miocene granite formation by detachment tectonics or not? A case study from the northern Menderes Massif (Western Turkey). *Journal of Geodynamics* **50**, 67-80.

Hetzel, R. & Reischmann, T. (1996). Intrusion age of Pan-African augen gneisses in the southern Menderes Massif and the age of cooling after Alpine ductile extensional deformation. *Geological Magazine* **133**, 565-572.

Hetzel, R., Ring, U., Akal, C. & Troesch, M. (1995). Miocene NNE-Directed Extensional Unroofing in the Menderes-Massif, Southwestern Turkey. *Journal of the Geological Society* **152**, 639-654.

Işık, V., Tekeli, O. & Seyitoglu, G. (2004). The $^{40}Ar/^{39}Ar$ age of extensional ductile deformation and granitoid intrusion in the northern Menderes core complex: implications for the initiation of extensional tectonics in western Turkey. *Journal of Asian Earth Sciences* **23**, 555-566.

Jochum, K. P., Willbold, M., Raczek, I., Stoll, B. & Herwig, K. (2005). Chemical characterisation of the USGS reference glasses GSA-1G, GSC-1G, GSD-1G, GSE-1G, BCR-2G, BHVO-2G and BIR-1G using EPMA, ID-TIMS, ID-ICP-MS and LA-ICP-MS. *Geostandards and Geoanalytical Research* **29**, 285-302.

Johnson, M. C. & Rutherford, M. J. (1989). Experimental calibration of the aluminum-in-hornblende geobarometer with application to Long Valley caldera (California) volcanic rocks. *Geology* **17**, 837-841.

Jolivet, L. & Brun, J. P. (2010). Cenozoic geodynamic evolution of the Aegean. *International Journal of Earth Sciences* **99**, 109-138.

Koralay, O. E. (2015). Late Neoproterozoic granulite facies metamorphism in the Menderes Massif, Western Anatolia/Turkey: implication for the assembly of Gondwana. Geodinamica Acta **27**, 244-266.

Konstantinou, A., Strickland, A., Miller, E., Vervoort, J., Fisher, C. M., Wooden, J. & Valley, J. (2013). Synextensional magmatism leading to crustal flow in the Albion–Raft River–Grouse Creek metamorphic core complex, northeastern Basin and Range. *Tectonics* **32**, 1384-1403.

Le Maitre, R. W. (ed.) (2002). *Igneous Rocks: A Classification and Glossary of Terms: Recommendations of the International Union of Geological Sciences Subcommission on the Systematics of Igneous Rocks*. Cambridge: Cambridge University Press

Li, W., Costa, F. & Nagashima, K. (2020). Apatite Crystals Reveal Melt Volatile Budgets and Magma Storage Depths at Merapi Volcano, Indonesia. *Journal of Petrology* **62**, 1-35.

Lips, A. L. W., Cassard, D., Sözbilir, H., Yilmaz, H. & Wijbrans, J. R. (2001). Multistage exhumation of the Menderes Massif, western Anatolia (Turkey). *International Journal of Earth Sciences* **89**, 781-792.

Lister, G. S. & Davis, G. A. (1989). The origin of metamorphic core complexes and detachment faults formed during Tertiary continental extension in the northern Colorado River region, U.S.A. *Journal of Structural Geology* **11**, 65-94.

Ludwig, K. R. (2003). User's Manual for Isoplot 3.00 : a Geochronological Toolkit for Microsoft Excel.

Makris, J. & Stobbe, C. (1984). Physical properties and state of the crust and upper mantle of the Eastern Mediterranean Sea deduced from geophysical data. *Marine Geology* **55**, 347-363.

Mallik, A., Dasgupta, R., Tsuno, K. & Nelson, J. (2016). Effects of water, depth and temperature on partial melting of mantle-wedge fluxed by hydrous sediment-melt in subduction zones. *Geochimica Et Cosmochimica Acta* **195**, 226-243.

McDonough, W.F. & Sun, S.-S. (1995). Composition of the Earth. Chemical Geology 120, 223-253.

Miller, E. L., Calvert, A. T. & Little, T. A. (1992). Strain-collapsed metamorphic isograds in a sillimanite gneiss dome, Seward Peninsula, Alaska. *Geology* **20**, 487-490.

Mitchell, R. H. (1994). The lamprophyre facies. *Mineralogy and Petrology* **51**, 137-146.

Meulenkamp, J. E., Wortel, M. J. R., van Wamel, W. A., Spakman, W. & Hoogerduyn Strating, E. (1988). On the Hellenic subduction zone and the geodynamic evolution of Crete since the late Middle Miocene. *Tectonophysics* **146**, 203-215.

Nehring, F., Jacob, D. E., Barth, M. G. & Foley, S. F. (2008). Laser-ablation ICP-MS analysis of siliceous rock glasses fused on an iridium strip heater using MgO dilution. *Microchimica Acta* **160**, 153-163.

Nandedkar, R., Hurlimann, N., Ulmer, P. & Müntener, O. (2016). Amphibole–melt trace element partitioning of fractionating calc-alkaline magmas in the lower crust: an experimental study. *Contributions to Mineralogy and Petrology* **171**, 71.

Nilius, N.-P., Glotzbach, C., Wölfler, A., Hampel, A., Dunkl, I., Akal, C., Heineke, C. & Hetzel, R. (2019). Exhumation history of the Aydın range and the role of the Büyük Menderes detachment system during bivergent extension of the central Menderes Massif, western Turkey. *Journal of the Geological Society* **176**.

Okay, A. I. (2001). Stratigraphic and metamorphic inversions in the central Menderes Massif: a new structural model. *International Journal of Earth Sciences* **89**, 709-727.

Okay, A. & Tuysuz, O. (1999). Tethyan Sutures of northern Turkey. *Geological Society London Special Publications* **156**, 475-515.

Okay, A. & Nikishin, A. (2015). Tectonic evolution of the southern margin of Laurasia in the Black Sea region. *International Geology Review* **57**, 5-8.

Okay, A.I., Satır, M., Tüysüz, O., Akyüz, S., & Chen, F., 2001, The tectonics of the Strandja Massif: Late-Variscan and mid-Mesozoic deformation and metamorphism in the northernAegean: International Journal of Earth Sciences 90, 217–233.

Oner, Z., Dilek, Y. & Kadioglu, Y. K. (2010). Geology and geochemistry of the synextensional Salihli granitoid in the Menderes core complex, western Anatolia, Turkey. *International Geology Review* **52**, 336-368.

Pearce, N. J. G., Perkins, W. T., Westgate, J. A., Gorton, M. P., Jackson, S. E., Neal, C. R. & Chenery, S. P. (1997). A compilation of new and published major and trace element data for NIST SRM 610 and NIST SRM 612 glass reference materials. *Geostandards Newsletters* **21**, 115-144.

Petford, N. & Gallagher, K. (2001). Partial melting of mafic (amphibolitic) lower crust by periodic influx of basaltic magma. *Earth and Planetary Science Letters* **193**, 483-499.

Pouchou, J. L. & Pichoir, F. (1984). A new model for quantitative analysis. 1. Application to the analysis of homogeneous samples. *Recherche Aérospatiales* **5**, 47-65.

Prelević , D., Akal, C., Foley, S. F., Romer, R. L., Stracke, A. & Van Den Bogaard, P. (2012). Ultrapotassic Mafic Rocks as Geochemical Proxies for Post-collisional Dynamics of Orogenic Lithospheric Mantle: the Case of Southwestern Anatolia, Turkey. *Journal of Petrology* **53**, 1019-1055.

Prelević, D., Akal, C., Romer, R. & Foley, S. F. (2010). Lamproites as indicators of accretion and/or shallow subduction in the assembly of Southwestern Anatolia, Turkey. *Terra Nova* **22**, 443–452.

Prelević , D., Akal, C., Romer, R. L., Mertz-Kraus, R. & Helvaci, C. (2015). Magmatic Response to Slab Tearing: Constraints from the Afyon Alkaline Volcanic Complex, Western Turkey. *Journal of Petrology* **56**, 527-562.

Prelević, D., Foley, S. F., Cvetković, V. & Romer, R. L. (2004). Origin of Minette by Mixing of Lamproite and Dacite Magmas in Veliki Majdan, Serbia. *Journal of Petrology* **45**, 759-792.

Prelević, D., Foley, S. F., Romer, R. & Conticelli, S. (2008). Mediterranean tertiary lamproites derived from multiple source components in postcollisional geodynamics. *Geochimica Et Cosmochimica Acta* **72**, 2125-2156.

Prelević , D., Jacob, D. E. & Foley, S. F. (2013). Recycling plus: A new recipe for the formation of Alpine-Himalayan orogenic mantle lithosphere. *Earth and Planetary Science Letters* **362**, 187-197.

Putirka, K. D., Mikaelian, H., Ryerson, F. & Shaw, H. (2003). New clinopyroxene-liquid thermobarometers for mafic, evolved, and volatile-bearing lava compositions, with applications to lavas from Tibet and the Snake River Plain, Idaho. *American Mineralogist* **88**, 1542-1554.

Putirka, K. D. (2008). Thermometers and Barometers for Volcanic Systems. *Minerals, Inclusions and Volcanic Processes* **69**, 61-120.

Putirka, K. (2016). Amphibole thermometers and barometers for igneous systems and some implications for eruption mechanisms of felsic magmas at arc volcanoes. *American Mineralogist* **101**, 841-858.

Ridolfi, F. & Renzulli, A. (2012). Calcic amphiboles in calc-alkaline and alkaline magmas: thermobarometric and chemometric empirical equations valid up to 1,130A degrees C and 2.2 GPa. *Contributions to Mineralogy and Petrology* **163**, 877-895.

Ridolfi, F., Renzulli, A. & Puerini, M. (2010). Stability and chemical equilibrium of amphibole in calc-alkaline magmas: an overview, new thermobarometric formulations and application to subduction-related volcanoes. *Contributions to Mineralogy and Petrology* **160**, 45-66.

Rimmelé, G., Oberhänsli, R., Goffé, B., Jolivet, L., Candan, O. & Çetinkaplan, M. (2003). First evidence of high-pressure metamorphism in the "Cover Series" of the southern Menderes Massif. Tectonic and metamorphic implications for the evolution of SW Turkey. *Lithos* **71**, 19-46.

Robertson, A. H. F. & Ustaömer, T. (2009). Upper Palaeozoic subduction/accretion processes in the closure of Palaeotethys: Evidence from the Chios Melange (E Greece), the Karaburun Melange (W Turkey) and the Teke Dere Unit (SW Turkey). *Sedimentary Geology* **220**, 29-59.

Rock, N. M. S. (1977). The nature and origin of lamprophyres: some definitions, distinctions, and derivations. *Earth Science Reviews* **13**, 123-169.

Rock, N. M. S. (1983). Nature and origin of calc-alkaline lamprophyres; minettes, vogesites, kersantites and spessartites. *Transactions of the Royal Society of Edinburgh: Earth Sciences*.

Rock, N. M. S. (1991). *Lamprophyres*. Glasgow: Blackie and Son Ltd.

Scarrow, J. H., Bea, F., Montero, P. & Molina, J. F. (2009). Shoshonites, vaugnerites and potassic lamprophyres: similarities and differences between 'ultra'-high-K rocks. *Earth and Environmental Science Transactions of the Royal Society of Edinburgh* **99**, 159-175.

Schmidt, M. W. (1992). Amphibole composition in tonalite as a function of pressure: an experimental calibration of the Al-in-hornblende barometer. *Contributions to Mineralogy and Petrology* **110**, 304-310.

Sekine, T. & Wyllie, P. J. (1982). The system granite-peridotite-H_2O at 30 kbar, with applications to hybridization in subduction zone magmatism. *Contributions to Mineralogy and Petrology* **81**, 190.

Şengör, A. M. C. (1984). The Cimmeride Orogenic System and the Tectonics of Eurasia. *The Cimmeride Orogenic System and the Tectonics of Eurasia*. Special Paper - Geological Society of America **195**, 82 pp.

Şengör, A. M. C., Görür, N. & Saroglu, F. (1985). Strike-slip faulting and related basin formation in zones of tectonic escape: Turkey as a case study. In: Biddle, K. T. & Christie-Blick, N. (eds.) *Strike-Slip Deformation, Basin Formation, and Sedimentation*. Kluwer Academic Publishers Dordrecht / Boston / London: Society of Economic Paleontologists and Mineralogists, 227–264.

Şengör, A. M. C. & Yilmaz, Y. (1981). Tethyan evolution of Turkey: A plate tectonic approach. *Tectonophysics* **75**, 181-241.

Şengör, A. M. C.; Satir, M. & Akkök, R. (1984) Timing of tectonic events in the Menderes Massif, western Turkey: Implications for tectonic evolution and evidence for pan-African basement in Turkey. Tectonics **3**, 693-707.

Sheppard, S. (1995). Hybridization of shoshonitic lamprophyre and calc-alkaline granite magma in the early Proterozoic Mt Bundey igneous suite, Northern Territory. *Australian Journal of Earth Sciences* **42**, 173-185.

Soder, C., Altherr, R. & Romer, R. L. (2016). Mantle Metasomatism at the Edge of a Retreating Subduction Zone: Late Neogene Lamprophyres from the Island of Kos, Greece. *Journal of Petrology* **57**, 1705-1728.

Stoll, B., Jochum, K. P., Herwig, K., Amini, M., Flanz, M., Kreuzburg, B., Kuzmin, D., Willbold, M. & Enzweiler, J. (2008). An Automated Iridium-Strip Heater for LA-ICP-MS Bulk Analysis of Geological Samples. *Geostandards and Geoanalytical Research* **32**, 5–26. .

Stracke, A., Hofmann, A. W. & Hart, S. R. (2005). FOZO, HIMU, and the rest of the mantle zoo. Geochemistry Geophysics Geosystems 6.

Sun, S. S. & McDonough, W. F. (1989). Chemical and isotopic systematics of oceanic basalts; implications for mantle composition and processes. In: Saunders, A. D. & Norry, M. J. (eds.) Magmatism in the ocean basins. London, United Kingdom: Geological Society of London, 313-345.

Tappe, S., Foley, S. F., Jenner, G. A. & Kjarsgaard, B. A. (2005). Integrating Ultramafic Lamprophyres into the IUGS Classification of Igneous Rocks: Rationale and Implications. *Journal of Petrology* **46**, 1893-1900.

van Hinsbergen, D. J. J., Hafkenscheid, E., Spakman, W., Meulenkamp, J. E. & Wortel, R. (2005). Nappe stacking resulting from continental lithosphere below subduction of oceanic and Greece. *Geology* **33**, 325-328.

Wang, Y., Foley, S. F. & Prelević, D. (2017). Potassium-rich magmatism from a phlogopite-free source. *Geology* **45**, 467-470.

Wimmenauer, W. (1973). Lamprophyre, Semilamprophyre und anchibasaltsche Ganggesteine. *Fortschritte Der Mineralogie* **51**, 3-67.

Woolley, A. R., Bergman, S. C., Edgar, A. D., Le Bas, M. J., Mitchell, R., H., Rock, N. M. S. & Scott Smith, B. H. (1996). Classification of Lamprophyres, Lamproites, Kimberlites, and Kalsilitic, Melilitic, and Leucitic rocks. *The Canadian Mineralogist* **34**, 175-186.

Wortel, M. J. R. & Spakman, W. (2000). Subduction and Slab Detachment in the Mediterranean-Carpathian Region. *Science* **290**, 1910-1917.

Yılmaz, Y., Genc, S. C., Gurer, F., Bozcu, M., Yilmaz, K., Karacik, Z., Altunkaynak, S. & Elmas, A. (2000). When Did the Western Anatolian Grabens Begin to Develop? *Geological Society, London, Special Publications* **173**, 353-384.

Zeh, A., Gerdes, A., Klemd, R. & Barton, J. M., Jr. (2007). Archaean to Proterozoic Crustal Evolution in the Central Zone of the Limpopo Belt (South Africa-Botswana): Constraints from Combined U-Pb and Lu-Hf Isotope Analyses of Zircon. *J. Petrology* **48**, 1605-1639.

Zhu, L., Mitchell, B. J., Akyol, N., Cemen, I. & Kekovali, K. (2006). Crustal thickness variations in the Aegean region and implications for the extension of continental crust. *Journal of Geophysical Research: Solid Earth* **111**.

Zindler, A. & Hart, S. (1986). Chemical geodynamics. *Annual Review of Earth and Planetary Sciences* **14**, 493-571.

FIGURE CAPTION

Figure 1. Simplified geological map of the Menderes Massif with the study area marked by a rectangle. The inset at the bottom right shows the location of the map in the Eastern Mediterranean region. Map modified after Okay (2001) and Candan et al (2011).

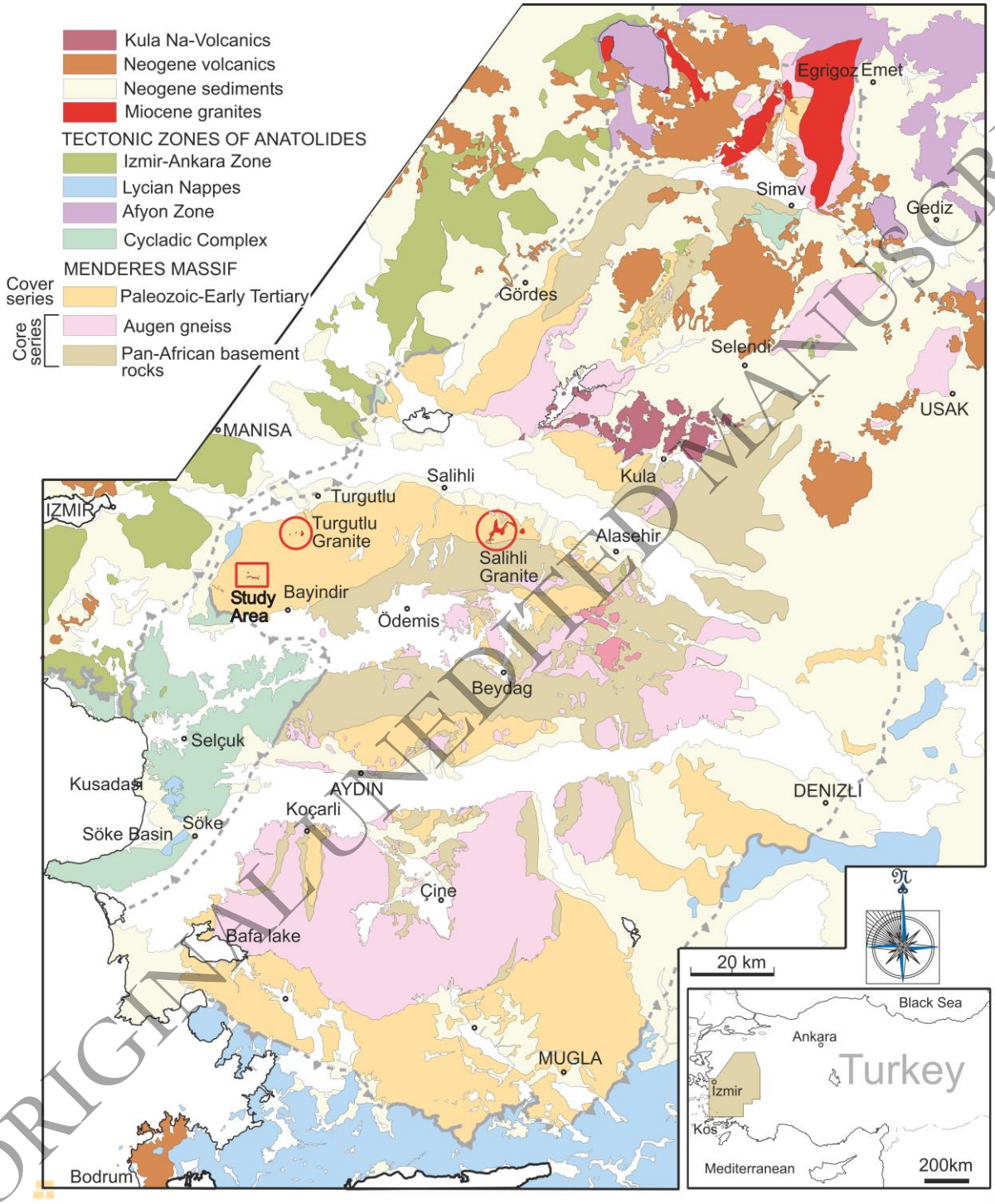

Figure 2. a) Aerial photograph (taken from Google Earth) with sample locations and grouping of samples into separate sills (for exact localities see Table 1); b) Representative field photograph of sill 1 illustrating outcrop conditions and the characteristic sharp contact between sill and country rocks; c) characteristic exfoliation of sills makes it easy to distinguish them from the schistose country rocks (hammer for scale is 35 cm long).

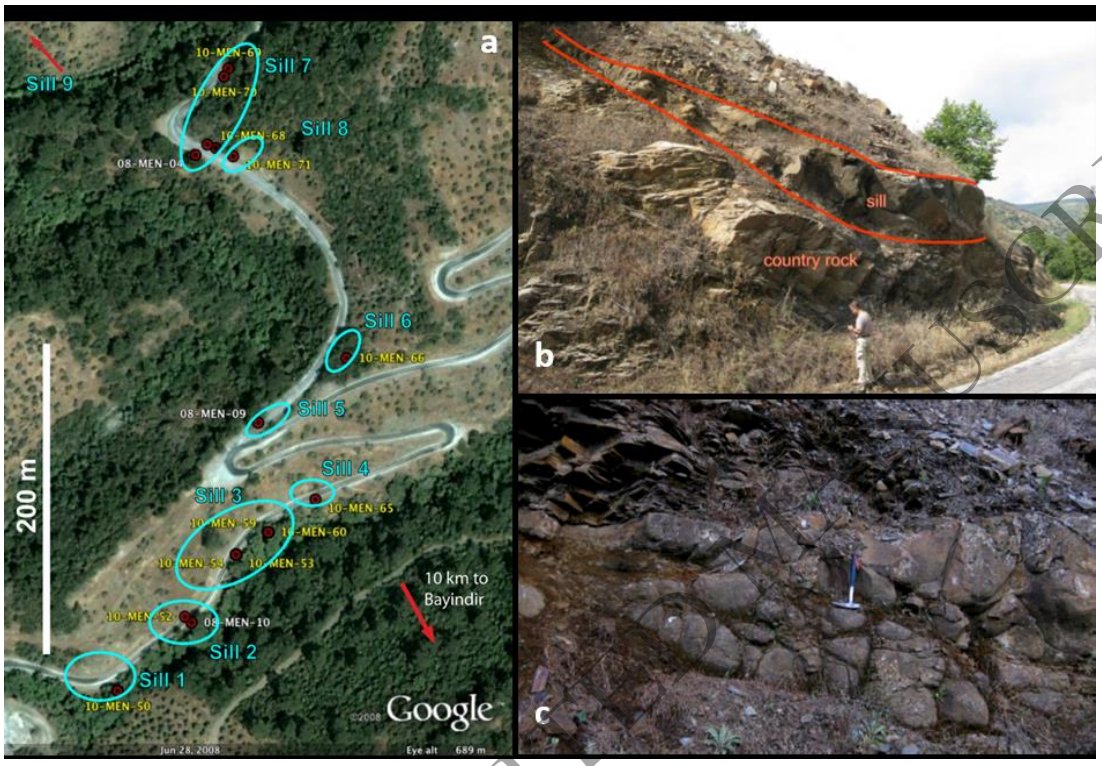

Figure 3. BSE images of typical a) biotite phenocryst; b) zoned amphibole phenocryst; c) subhedral orthopyroxene (left) next to smaller, patchy clinopyroxene; d) groundmass with zoned and euhedral plagioclase + anhedral quartz (black) + anhedral K-feldspar (grey, altered) and biotite phenocrysts; e) clinopyroxene microcrystals around a carbonate fragment; f) clinopyroxene microcrystals around quartz xenocryst (note K-feldspar at lower right contact); g) and h) clinopyroxene cluster without apparent nucleus.

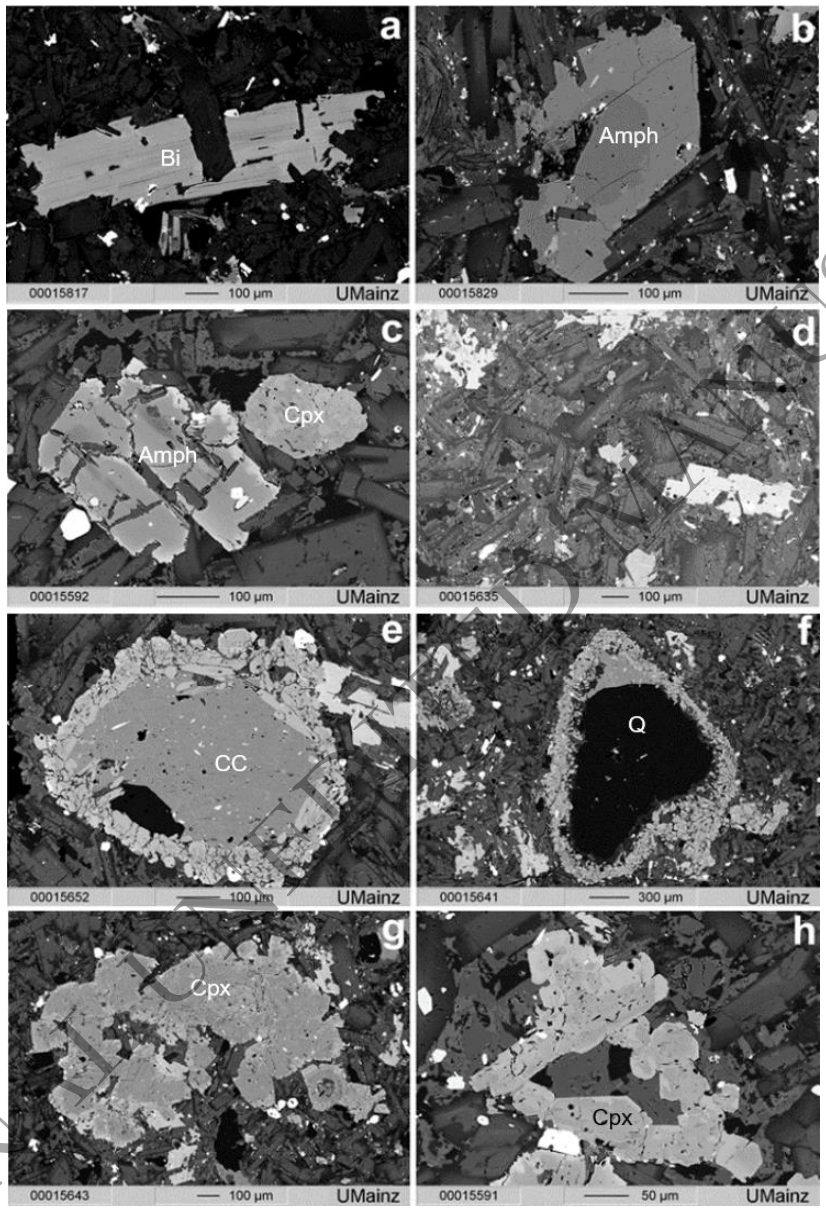

Figure 4. The BSE images show compositional zonation of amphibole (a) and clinopyroxene (b) phenocrysts. The arrow on the images refers to the EMPA major element analysis line scan (values in wt%) shown to the right of the BSE images. Circles in the BSE images mark position of the LA-ICP-MS trace element REE analyses shown below the BSE images. REE data normalized to chondrite values of McDonough & Sun (1995).

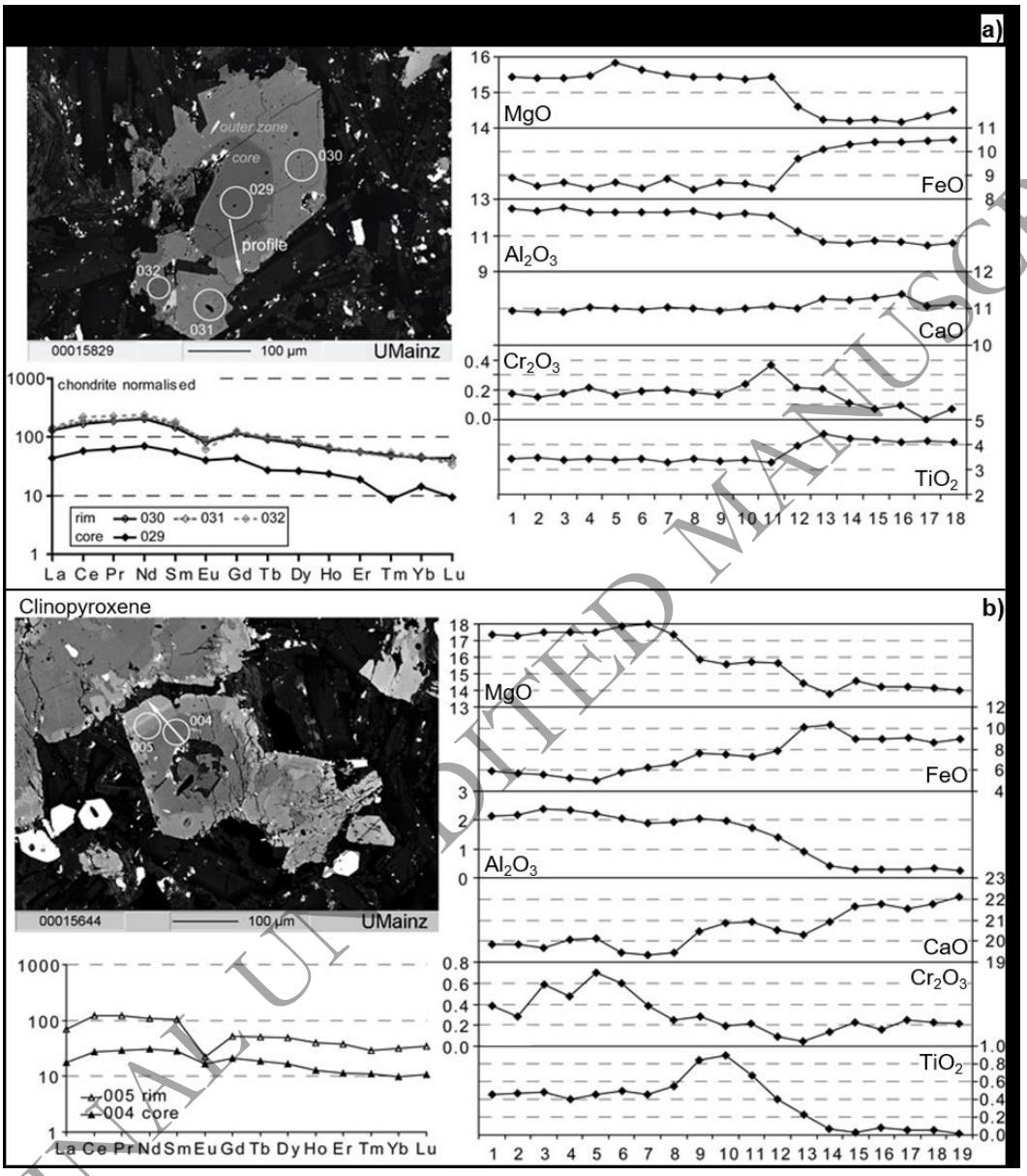

Figure 5. Trace element concentration (in ppm) vs. Mg# for amphibole. Mg# and contents of most trace elements differ markedly beween core and rim.

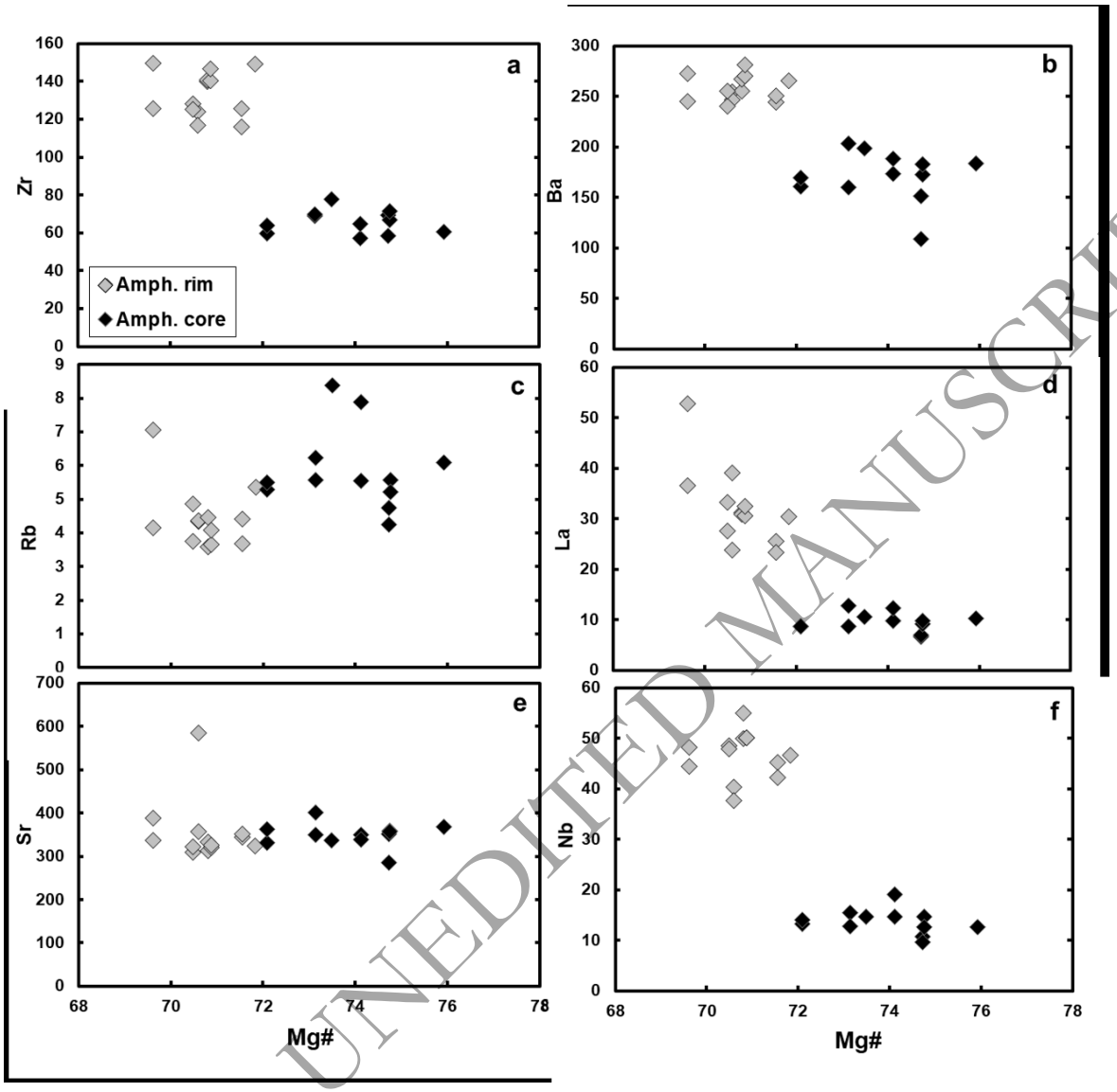

Figure 6. Trace element ratios vs. Mg# for amphibole and clinopyroxene. Clinopyroxene core and clinopyroxene rim refer to Group I, and patchy to Group II clinopyroxene (see Figure 3c). $Eu/Eu^* = Eu_N/(\sqrt{Sm_N} \times Gd_N)$.

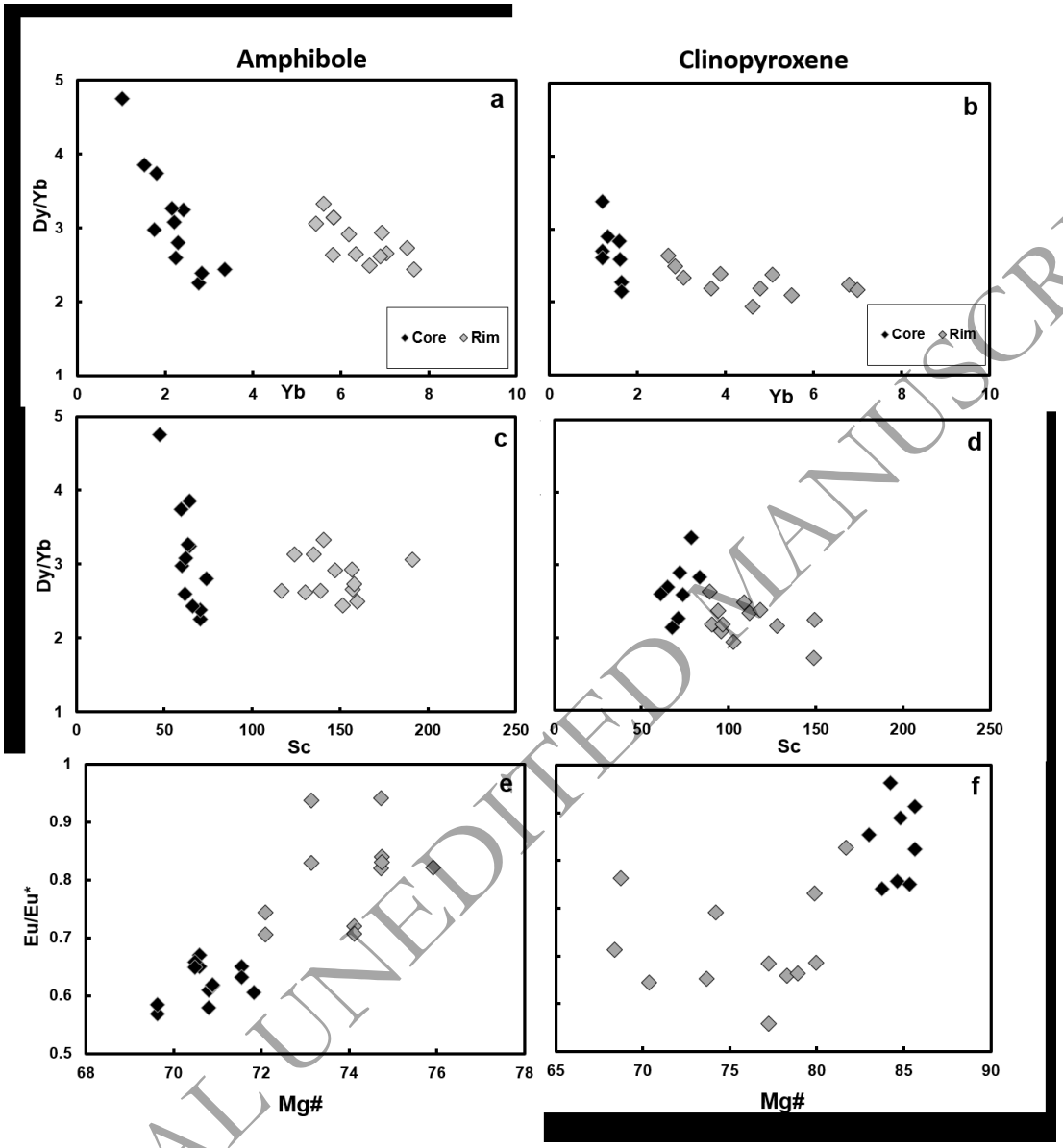

Figure 7. a) □Hf vs. $^{176}Lu/^{177}Hf$ composition of zircons retrieved from the Menderes lamprophyres. Error bars denote ± 1□□□□□; Turkish ultra-K lavas from Prelević et al. (2010); b) Geochemical classification of the lamprophyric rocks on the TAS diagram (lines and fields from Le Maitre, 2002).

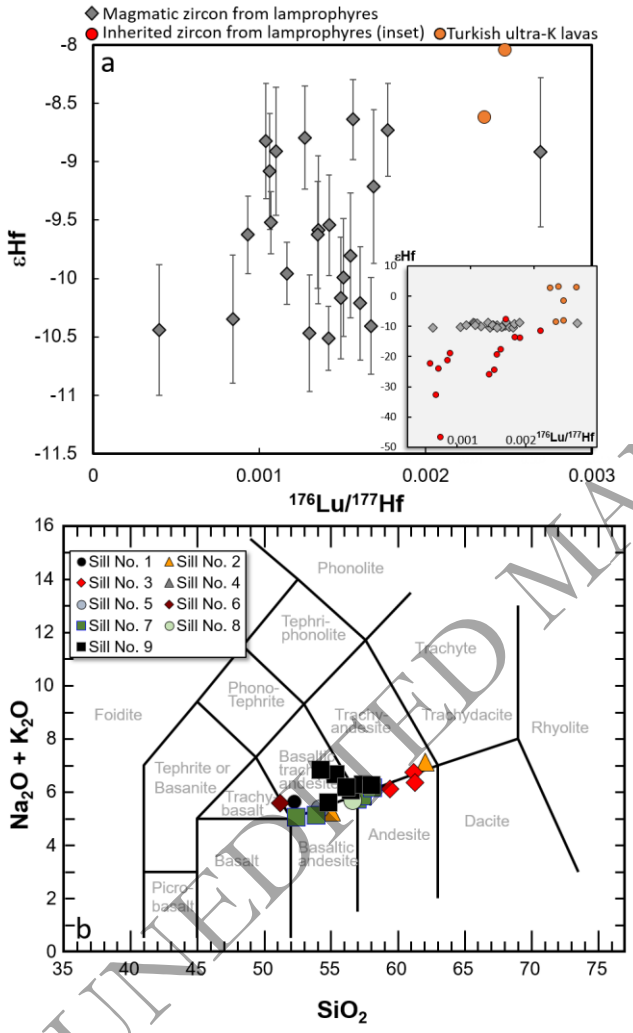

Figure 8. Whole-rock major element variation diagrams for Menderes lamprophyres. Data for Salihli and Turgutlu granitoids from Erkül & Erkül (2012), Erkül et al., (2013); data for metaigneous rocks from the Cadomian basement from Bozkurt et al. (2006), Gürsu (2016), Koralay et al. (2015) and references therein. The sample of augen gneiss xenolith is 10MEN61x.

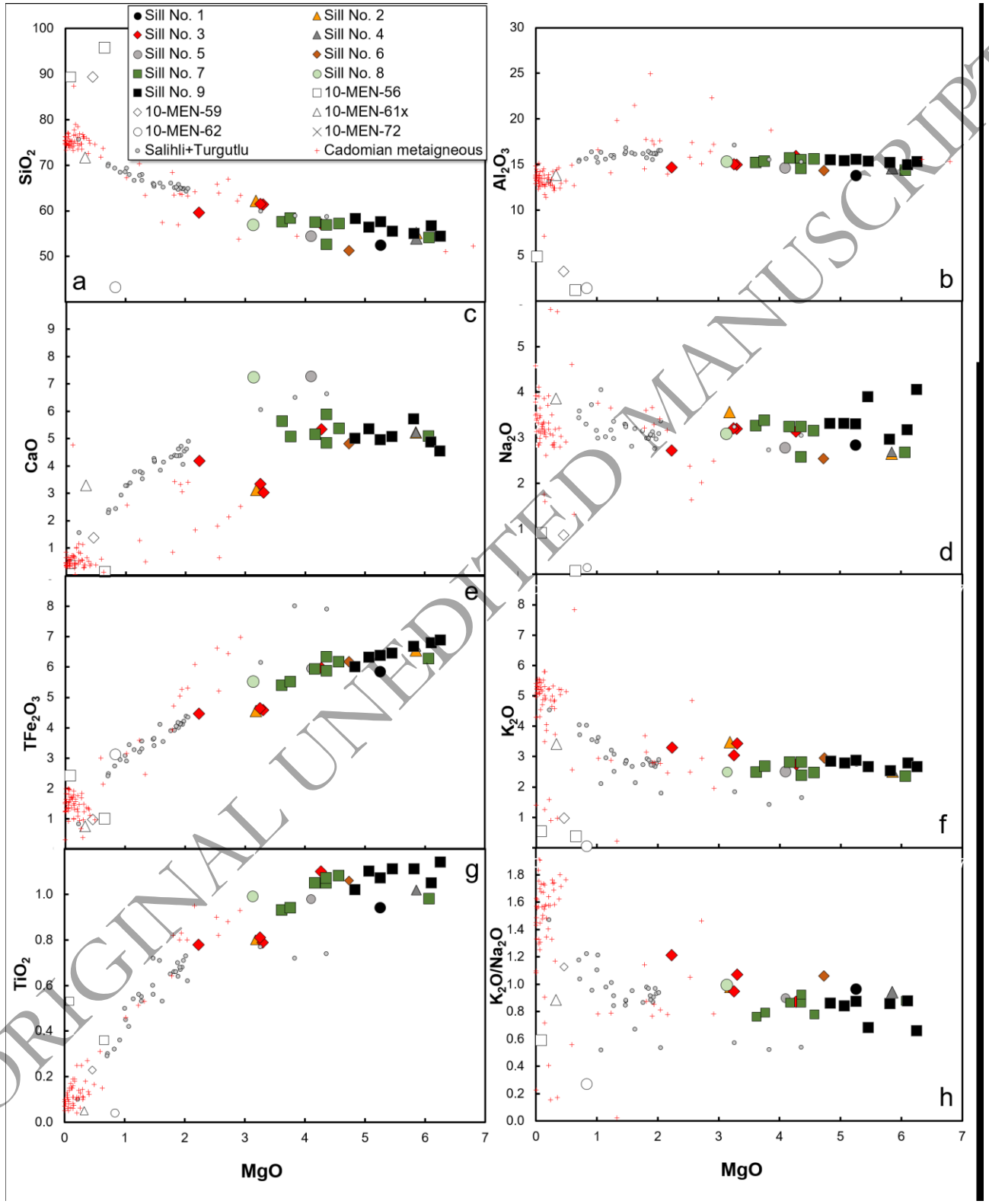

Figure 9. Plots of whole-rock trace element concentrations vs. MgO for Menderes lamprophyres. Data sources as in Figure 8.

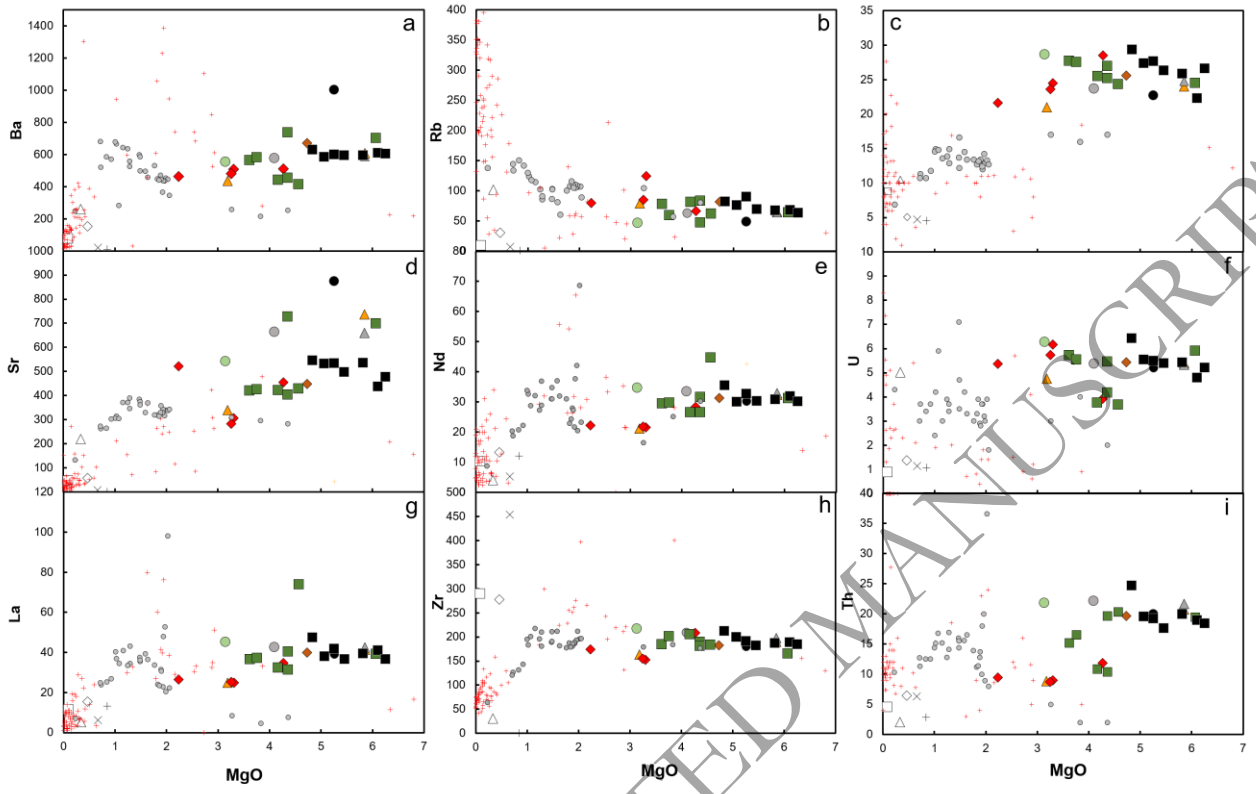

Figure 10. Plots of whole-rock trace-element ratios vs. MgO for Menderes lamprophyres. Symbols and data sources as in Figure 8.

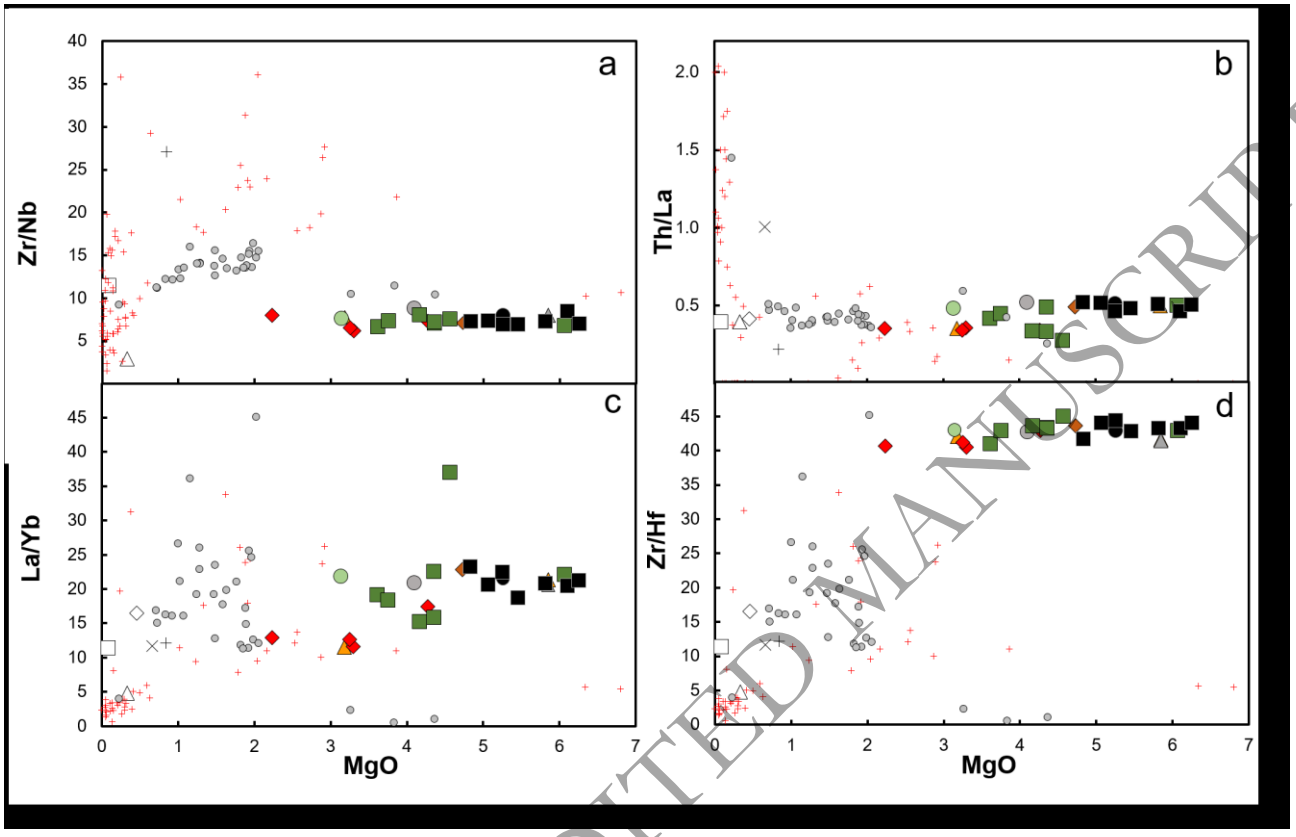

Figure 11. Variation diagram ('spidergram') for incompatible trace element (a) and REE contents (b) of whole-rock samples, normalised to the primitive mantle and chondrites of Sun & McDonough (1989). Data sources: Lamprophyres and xenoliths (including augen gneiss xenolith 10MEN61x) from this study, Menderes granitoids from Erkül & Erkül (2012), Kos volcanics from Soder et al. (2016), Santorini from Bailey et al. (2009 and references therein).

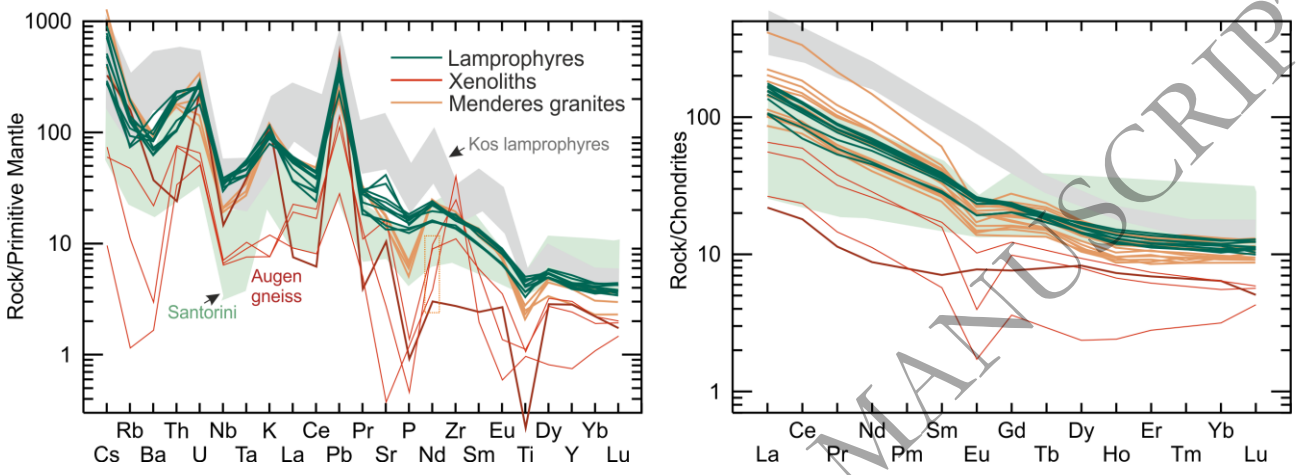

Figure 12. a) Plot of Sr vs. Nd isotopic compositions of the Menderes lamprophyres. All values are initial values. The Sr isotopic composition of the leachates is combined with the Nd isotopic composition of the unleached samples. The sample of augen gneiss is 10MEN61x. Note that the Sr isotopic composition of the calc-silicate xenolith and its leachate are within analytical uncertainties identical. b) and c) Plots of Pb vs. Pb isotopic compositions. All values are initial values. Northern Hemisphere Reference Line (NHRL) calculated using the formula from Hart (1984). Data sources: Lamprophyres and xenoliths from this study, Menderes granitoids from Erkül & Erkül (2012), Erkül et al., (2013), Kula volcanics from Alıcı et al. (2002), Turkish volcanic rocks from Prelević et al., 2015 and references therein, Cadomian metaigneous from Gürsu (2016)

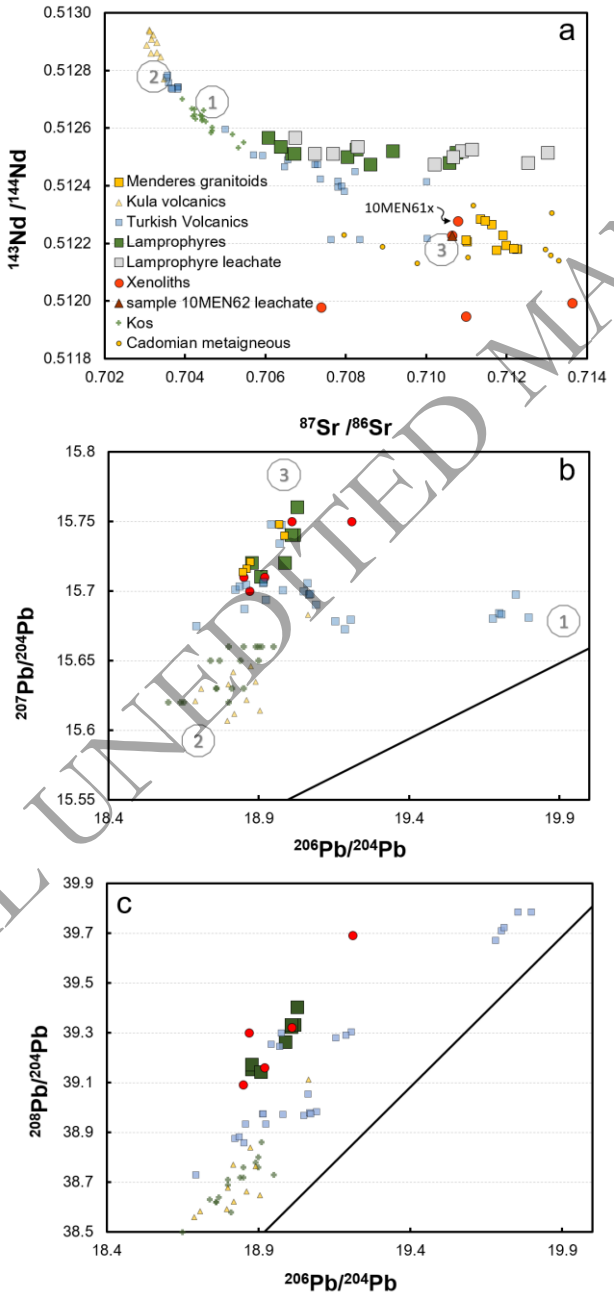

Figure 13. a) Plot of Mg# vs. T (°C) and b) depth (km) estimates using amphibole compositions and the model of Ridolfi et al. (2010, 2012).

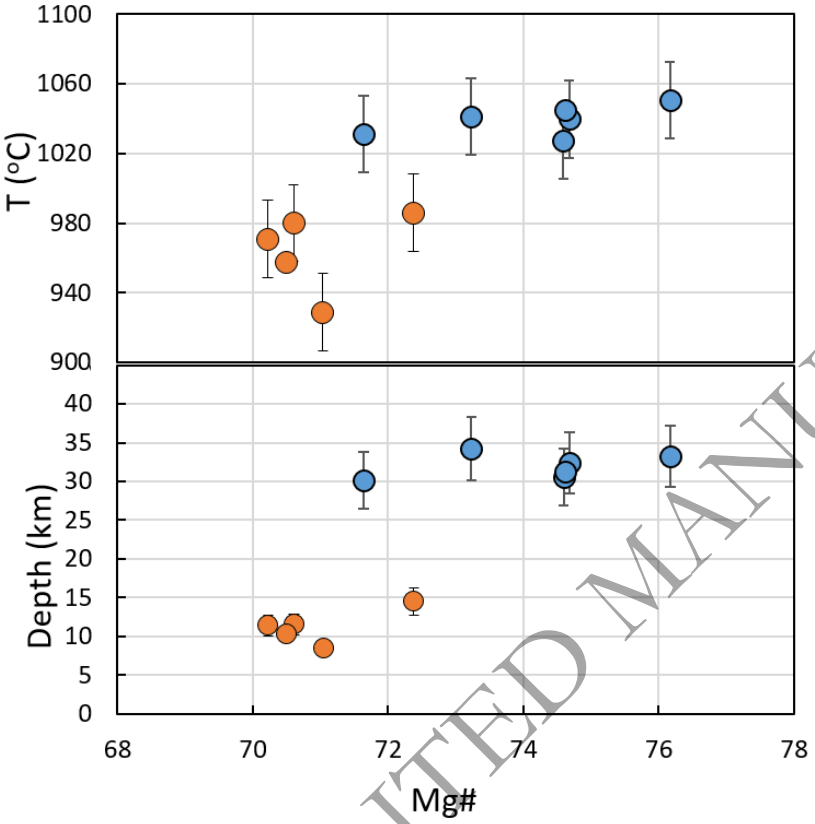

Figure 14. Age vs. □Nd for Menderes granitic intrusions. The plot implies a causality between the geochemistry of the granites and the basement rocks, as part of the general N-S younging trend shown by W. Anatolian magmatism (see text for further discussion). Data sources: Menderes granitoids from Erkül & Erkül (2012), Erkül et al., (2013); Turkish basaltic volcanic rocks from Prelević et al. (2015) and references therein, and Ersoy et al., (2008); Cadomian metaigneous (augen gneiss) and metasediments from Avigad et al. (2016).

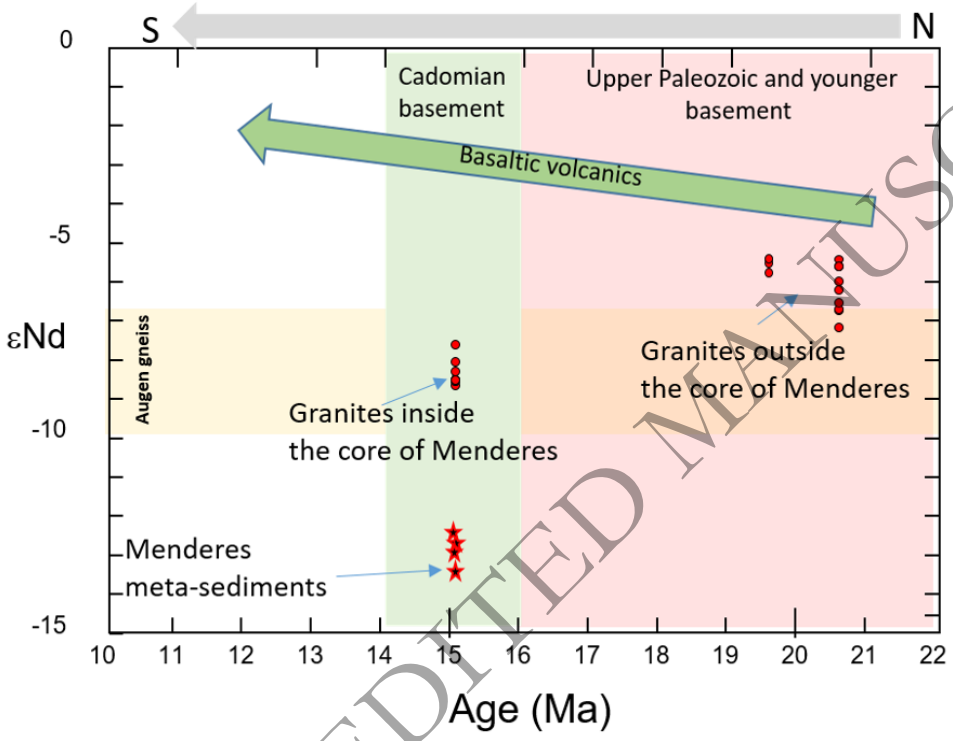

Figure 15. Evolution model for lamprophyric magmatism within the Menderes metamorphic core complex. See text for detailed discussion. The columnar section of the Menderes Massif is modified from Candan et al., (2011).

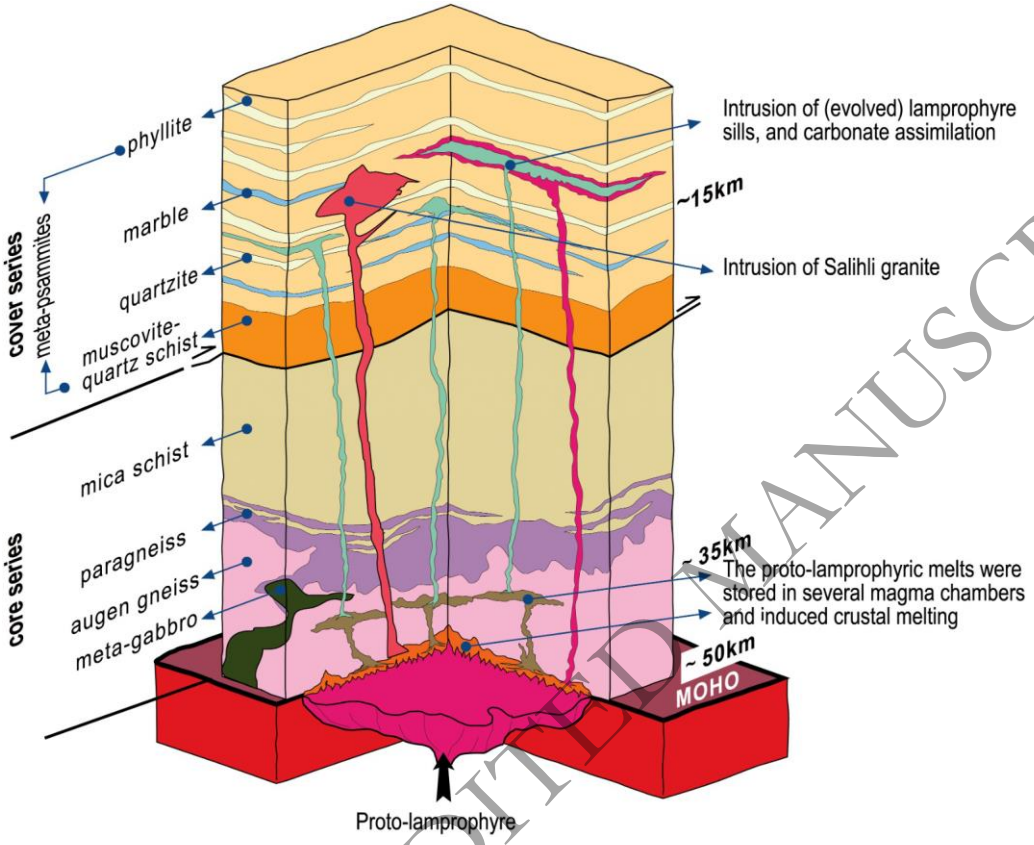

Table 1: Hf isotopes from MC-LA-ICP-MS analysis of zircons

Sample Name	$^{176}Yb/^{177}Hf$[a]	±2σ	$^{176}Lu/^{177}Hf$[a]	±2σ	$^{176}Lu/^{177}Hf$[a]	$^{180}Hf/^{177}Hf$[a]	SigHf[b] [V]	$^{176}Hf/^{177}Hf$	±2σ[c]	$^{176}Hf/^{177}Hf_i$[d]	εHfi[d]	±2σ[c]	TNC[e] [Ga]	age[f] [Ma]
68-seq1-A06	0.0204	21	0.00084	7	1.46718	1.88657	6	0.282483	31	0.282483	-10.4	1.1	1.28	15
68-seq1-A11	0.0385	42	0.0015	14	1.46714	1.8869	5	0.282493	29	0.282493	-10	1	1.26	15
68-seq1-A13	0.0412	42	0.00178	15	1.46716	1.88679	4	0.282386	29	0.282352	7.1	1	1.13	1002
68-seq1-A14	0.0348	39	0.00142	14	1.46718	1.88682	8	0.282506	24	0.282506	-9.6	0.9	1.23	15
68-seq1-A14b	0.0331	59	0.0013	20	1.46722	1.88669	7	0.28248	28	0.28248	-10.5	1	1.28	15
68-seq1-A20	0.0404	34	0.00155	10	1.4672	1.88651	5	0.282499	30	0.282498	-9.8	1.1	1.25	15
68-seq1-A20b	0.0419	37	0.00161	11	1.46721	1.88653	8	0.282487	27	0.282487	-10.2	1	1.27	15
68-seq1-A22	0.0703	79	0.00269	25	1.46721	1.8866	5	0.282524	36	0.282523	-8.9	1.3	1.2	15
68-seq2-A8	0.0087	11	0.0004	4	1.4672	1.88655	6	0.28248	32	0.28248	-10.5	1.1	1.28	14
68-seq2-A8core	0.0119	11	0.00045	4	1.46722	1.88681	5	0.281848	37	0.281843	-22.2	1.3	2.32	500
68-seq2-A52	0.0447	41	0.0017	12	1.46719	1.88661	6	0.282392	75	0.282383	-8.1	2.6	1.37	275
71-seq2-A22	0.0344	28	0.00156	10	1.4672	1.8865	9	0.28256	45	0.282537	8.9	1.6	0.86	788
71-seq2-A26	0.0409	55	0.00167	20	1.46725	1.8867	7	0.282482	23	0.282481	-10.4	0.8	1.28	15
71-seq2-A26b	0.0329	60	0.00135	22	1.46726	1.8866	9	0.282505	36	0.282505	-9.6	1.3	1.24	15
71-z01-seq2-A16	0.0522	48	0.0021	15	1.46718	1.88664	5	0.282452	37	0.282424	3.1	1.3	1.11	709
soil-z13-seq3	0.0348	29	0.00137	9	1.46715	1.88688	12	0.282087	23	0.282074	-14	0.8	1.88	500
soil-z13-seq3	0.0357	30	0.00142	9	1.46718	1.88668	11	0.282227	53	0.282213	-9.1	1.9	1.61	500
soil-z22-seq3	0.0128	12	0.00052	4	1.46715	1.88691	12	0.281455	21	0.28145	-36.1	0.7	3.07	500
soil-z24-seq3	0.031	39	0.00127	14	1.4672	1.88654	8	0.282527	25	0.282527	-8.8	0.9	1.19	15
soil-z24b-seq3	0.0383	44	0.00156	15	1.4672	1.88648	8	0.282532	19	0.282531	-8.6	0.7	1.18	15
soil-z27-seq3	0.0332	31	0.00135	10	1.46725	1.88665	7	0.282504	26	0.282503	-9.6	0.9	1.24	15
soil-z27b-seq3	0.0366	34	0.00149	11	1.46723	1.88674	7	0.282489	30	0.282488	-10.2	1	1.27	15
soil-z40-seq3	0.0135	11	0.0005	3	1.46722	1.88662	9	0.282098	20	0.282093	-13.3	0.7	1.84	500
soil-z41-seq3	0.2024	165	0.00732	46	1.46716	1.88672	13	0.282275	17	0.282206	-9.3	0.6	1.62	500
soil-z42-seq3	0.2399	346	0.00787	91	1.46714	1.8865	15	0.282497	40	0.282495	-9.9	1.4	1.25	15
soil-z52-seq3	0.0281	24	0.00104	7	1.46712	1.88691	5	0.282526	28	0.282526	-8.8	1	1.19	15
soil-z52b-seq3	0.0286	24	0.00106	7	1.4672	1.88667	8	0.282519	28	0.282519	-9.1	1	1.21	15
soil-z64-seq3	0.0103	10	0.00036	3	1.46712	1.88673	5	0.282144	33	0.282138	-2.7	1.2	1.59	900
soil-z65-seq3	0.0284	29	0.0011	9	1.46723	1.88679	6	0.282524	31	0.282524	-8.9	1.1	1.2	15
soil-z67-seq3	0.0184	25	0.00068	8	1.46721	1.8866	9	0.282241	20	0.28223	0.5	0.7	1.41	900
soil-z73-seq3	0.0408	60	0.00169	22	1.46716	1.8867	7	0.282516	37	0.282515	-9.2	1.3	1.22	15
soil-z62-seq3	0.0158	14	0.00063	4	1.46714	1.88673	11	0.282176	154	0.282166	-1.8	5.5	1.54	900
soil-z89-seq3	0.0335	29	0.00148	10	1.46714	1.88678	11	0.282276	44	0.282276	-17.7	1.6	1.68	15

soil-z90-seq3	0.0252	22	0.00117	8	1.46724	1.88643	21	0.282494	15	0.282494	-10	0.5	1.26	15
soil-z90b-seq3	0.0222	20	0.00107	7	1.46715	1.8866	18	0.282507	15	0.282506	-9.5	0.5	1.23	15
soil-z90c-seq3	0.0257	22	0.00141	9	1.46722	1.8868	29	0.282479	16	0.282478	-10.5	0.5	1.29	15
soil-z99-seq3	0.0326	32	0.00129	10	1.46725	1.88651	6	0.282039	28	0.282039	-26.1	1	2.13	15
soil-z105-seq3	0.0376	33	0.00177	12	1.46726	1.8865	8	0.282529	22	0.282529	-8.7	0.8	1.19	15
soil-z105b-seq3	0.0194	16	0.00093	6	1.46721	1.88668	11	0.282504	19	0.282503	-9.6	0.7	1.24	15
Plesovice (n=8)	0.0039	36	0.0001	9	1.46715	1.88672	18	0.282482	14	0.282481	-3.2	0.5	1.15	338
GJ-1 (n=8)	0.0068	8	0.00027	1	1.46716	1.88669	13	0.282006	16	0.282003	-14.2	0.6	1.97	606
JMC 475 (n=6)					1.46718	1.8867	15	0.282148	8					

Quoted uncertainties (absolute) relate to the last quoted figure. The effect of the inter-element fractionation on the Lu/Hf ratio was estimated to be ≤ 6 %, based on analyses of the GJ-1 and Plesovice zircon. Accuracy and reproducibilty was checked by repeated analyses (n = 8 and 8, respectively) of reference zircon GJ-1 and Plesovice (data given as mean with 2 standard deviation uncertainties)

(a) $\left(\frac{^{176}\mathrm{Yb}}{^{177}\mathrm{Hf}}\right) = \left(\frac{^{176}\mathrm{Yb}}{^{173}\mathrm{Yb}}\right)_{\mathrm{true}} \times \left(\frac{^{173}\mathrm{Yb}}{^{177}\mathrm{Hf}}\right)_{\mathrm{meas}} \times \left(\frac{\mathrm{mass}(^{173}\mathrm{Yb})}{\mathrm{mass}(^{177}\mathrm{Hf})}\right)^{\mathrm{b(Hf)}}$ with $\mathrm{b(Hf)} = \ln\left(\frac{(^{179}\mathrm{Hf}/^{177}\mathrm{Hf})_{\mathrm{true}}}{(^{179}\mathrm{Hf}/^{177}\mathrm{Hf})_{\mathrm{meas}}}\right) \Big/ \ln\left(\frac{\mathrm{mass}(^{179}\mathrm{Hf})}{\mathrm{mass}(^{177}\mathrm{Hf})}\right)$

The ^{176}Lu=^{177}Hf were calculated in a similar way by using the ^{175}Lu=^{177}Hf and b(Yb).

(b) Mean Hf signal in volt.

(c) Uncertainties are quadratic additions of the within-run precision and the daily reproducibility of the 40ppb-JMC475 solution. Uncertainties for the JMC475 quoted at 2SD (2 standard deviation).

(d) Initial ^{176}Hf/^{177}Hf and εHf calculated using the apparent Pb-Pb age determined by LA-ICP-MS dating (see column age), and the CHUR parameters: ^{176}Lu/^{177}Hf = 0:0336, and ^{176}Hf/^{177}Hf = 0.282785 (Bouvier et al., 2008).

(e) two stage model age in billion years using the measured ^{176}Lu/^{177}Lu of each spot (first stage = age of zircon), a value of 0.0113 for the average continental crust (second stage), and a juvenile crust (NC) ^{176}Lu/^{177}Lu and ^{176}Hf/^{177}Hf of 0.0384 and 0.28314, respectively.

(f) apparent U-Pb age determined by LA-ICP-MS

Table 2: Results of the whole rock major and trace element data of Menderes lamprophyres and xenoliths

	Sample name	SiO2	Al2O3	Fe2O3	MnO	MgO	CaO	Na2O	K2O	TiO2	P2O5	SO3	Cr2O3	NiO	LOI	Sum	Mg#
	10-MEN-50	52.4	13.8	5.84	0.10	5.26	4.98	2.83	2.72	0.94	0.32	1.23	0.032	0.013	10.17	100.7	0.64
	08-MEN-10	62.3	15.4	4.56	0.09	3.18	3.13	3.56	3.47	0.80	0.30	0.080	0.011	0.005	3.84	100.7	0.58
	10-MEN-52	55.2	14.7	6.55	0.10	5.85	5.22	2.65	2.51	1.02	0.33	0.179	0.035	0.016	5.52	100.0	0.64
	10-MEN-53	59.7	14.7	4.46	0.08	2.23	4.19	2.72	3.30	0.78	0.28	0.249	0.010	0.004	7.53	100.3	0.50
	10-MEN-54a	61.5	15.0	4.58	0.09	3.30	3.03	3.20	3.43	0.79	0.27	0.070	0.012	0.005	4.67	99.9	0.59
	10-MEN-55	61. 6	15.1	4.64	0.09	3.25	3.34	3.21	3.04	0.81	0.29	0.102	0.012	0.005	4.66	100.1	0.58
	10-MEN-61h	57.1	16.0	5.97	0.08	4.27	5.34	3.14	2.74	1.10	0.37	0.288	0.018	0.008	3.66	100.1	0.59
	10-MEN-65	54.1	14.6	6.68	0.09	5.85	5.22	2.69	2.53	1.02	0.34	1.155	0.039	0.021	6.21	100.6	0.63
	08-MEN-09	54.4	14.6	5.96	0.12	4.10	7.26	2.77	2.49	0.98	0.35	0.440	0.032	0.015	6.54	100.1	0.58
	10-MEN-66	51.4	14.4	6.18	0.10	4.73	4.81	2.54	2.95	1.06	0.35	1.544	0.027	0.009	11.3	101.4	0.60
	08-MEN-05	57.6	15.7	5.93	0.09	4.17	5.15	3.23	2.80	1.05	0.37	0.080	0.017	0.007	3.65	99.8	0.58
	08-MEN-06	57.2	15.6	6.16	0.10	4.57	5.36	3.15	2.46	1.08	0.37	0.100	0.019	0.009	3.93	100.2	0.59
	09-MEN-16	56.9	15.5	5.86	0.11	4.36	4.83	3.23	2.80	1.05	0.37	0.114	0.017	0.007	4.10	99.3	0.60
	10-MEN-67	57.6	15.2	5.39	0.11	3.62	5.63	3.25	2.48	0.93	0.34	0.226	0.018	0.007	5.27	100.1	0.57
	10-MEN-68	58.4	15.4	5.50	0.09	3.76	5.06	3.37	2.67	0.94	0.33	0.211	0.018	0.007	4.66	100.4	0.58
	10-MEN-69	52.6	14.6	6.33	0.09	4.36	5.88	2.57	2.38	1.07	0.36	1.74	0.028	0.010	9.30	101.3	0.58
	10-MEN-70	54.1	14.4	6.26	0.10	6.07	5.08	2.67	2.35	0.98	0.32	0.237	0.035	0.016	7.54	100.2	0.66
	10-MEN-71	56.9	15.3	5.51	0.11	3.14	7.23	3.08	2.49	0.99	0.38	0.210	0.022	0.009	5.33	100.7	0.53
	08-MEN-08	56.8	15.0	6.79	0.18	6.11	4.87	3.17	2.77	1.05	0.37	0.250	0.034	0.015	2.94	100.3	0.64
	09-MEN-11	57.7	15.6	6.37	0.10	5.26	4.95	3.29	2.87	1.07	0.40	0.139	0.024	0.011	1.93	99.7	0.62
	09-MEN-12	55.6	15.4	6.45	0.11	5.46	5.06	3.89	2.65	1.11	0.38	0.016	0.027	0.013	3.26	99.4	0.63
	09-MEN-13	55.0	15.2	6.67	0.10	5.82	5.70	2.96	2.53	1.11	0.37	0.025	0.031	0.013	4.41	100.0	0.63
	09-MEN-14	56.4	15.4	6.31	0.10	5.07	5.35	3.30	2.77	1.10	0.36	0.118	0.022	0.009	3.27	99.6	0.61
	09-MEN-15	54.5	15.3	6.88	0.11	6.26	4.54	4.05	2.66	1.14	0.38	0.015	0.032	0.016	3.65	99.5	0.64
	10-MEN-73	58.3	15.5	6.00	0.10	4.84	4.99	3.30	2.83	1.02	0.37	0.128	0.023	0.009	2.39	99.8	0.61
Xenoliths	10-MEN-56	89.5	4.90	2.41	0.03	0.09	0.40	0.90	0.53	0.41	0.02	0.038	0.002	0.001	1.49	100.7	0.07
	10-MEN-59	89.5	3.33	0.98	0.04	0.46	1.37	0.86	0.97	0.23	0.01	0.008	0.001	0.001	1.50	99.3	0.48
	10-MEN-61x	71.9	13.9	0.76	0.06	0.33	3.29	3.86	3.42	0.05	0.02	0.010	n.d.	n.d.	2.23	99.8	0.46
	10-MEN-62	43.3	1.43	3.11	0.12	0.84	27.91	0.15	0.04	0.23	0.03	1.14	0.002	0.000	21.7	99.9	0.35
	10-MEN-72	95.9	1.24	1.00	0.04	0.66	0.11	0.07	0.36	0.41	n.d.	0.014	0.002	0.001	0.85	100.6	0.57

Measured by x-ray fluorescence. All values are in wt %. Fe_2O_3 is the total iron. n.d. = not detected. Mg# = MgO/(MgO+FeO), with oxides divided by molecular weight and FeO = Fe_2O_3*0.8998. Typical analytical uncertainties are given in Supplementary dataset 2.

Table 2: continued

	Sample name	Li	Sc	V	Cr	Ni	Rb	Sr	Y	Zr	Nb	Cs	Ba	Hf	Ta	Pb	Th	U
	10-MEN-50	22	15.8	84	223	86	49	874	18.6	180	22.7	2.21	1004	4.21	1.66	22	19.9	5.20
	08-MEN-10	44	15.1	63	102	36	79	340	23.6	163	21.0	4.04	435	3.88	2.24	30	8.88	4.76
	10-MEN-52	32	16.9	91	236	122	65	736	20.4	190	24.1	4.16	609	4.58	1.77	35	20.7	5.41
	10-MEN-53	46	14.5	65	84	32	80	521	20.5	174	21.7	7.28	465	4.27	2.21	33	9.45	5.36
	10-MEN-54a	62	14.2	75	84	34	124	307	20.0	153	24.6	7.17	508	3.77	2.28	27	8.96	6.16
	10-MEN-55	55	14.3	74	84	38	85	282	19.1	155	23.7	3.82	482	3.76	2.28	29	8.71	5.74
	10-MEN-61h	27	16.8	98	119	63	67	454	20.2	209	28.6	2.38	511	4.87	2.06	23	11.9	3.93
	10-MEN-65	38	17.2	92	282	132	64	660	19.9	198	24.8	3.24	588	4.77	1.82	28	21.7	5.34
	08-MEN-09	31	18.0	87	246	99	63	662	21.9	209	23.8	2.79	576	4.90	1.89	33	22.1	5.36
	10-MEN-66	31	15.8	99	183	63	82	448	18.0	183	25.7	5.82	670	4.19	1.68	27	19.7	5.43
	08-MEN-05	51	17.9	90	135	49	81	422	22.1	205	25.5	6.17	440	4.71	2.13	26	10.8	3.75
	08-MEN-06a	47	19.7	93	155	66	62	428	21.7	183	24.4	3.58	414	4.08	1.96	20	20.3	3.67
	08-MEN-06b	49	16.5	105	155	66	80	426	19.3	164	26.7	7.36	482	3.66	1.98	20	9.25	3.82
	09-MEN-16	68	16.9	96	127	50	83	402	20.6	189	27.0	5.63	454	4.37	2.13	22	10.4	4.17
	10-MEN-67	52	14.9	90	128	53	78	420	19.0	184	27.8	5.99	563	4.50	2.03	20	15.2	5.72
	10-MEN-68	52	14.9	84	130	52	59	425	20.2	201	27.6	2.3	581	4.69	2.09	16	16.5	5.53
	10-MEN-69	32	15.8	100	194	68	47	727	17.7	181	25.3	3.25	737	4.19	1.67	25	19.7	5.45
	10-MEN-70	27	14.9	96	260	108	64	699	17.6	165	24.5	18.0	701	3.85	1.62	28	19.5	5.89
	10-MEN-71	35	15.3	90	150	68	46	541	21.0	217	28.7	0.99	555	5.04	2.10	37	21.8	6.27
	08-MEN-08	74	19.1	92	245	113	67	437	21.8	188	22.3	4.24	609	4.36	1.71	66	18.9	4.78
	09-MEN-11	37	16.3	99	159	74	89	534	19.6	191	27.7	5.62	598	4.30	1.91	31	19.2	5.49
	09-MEN-12	44	18.0	103	199	101	69	496	19.7	181	26.4	2.16	593	4.24	1.88	29	17.6	5.39
	09-MEN-13	39	18.0	104	194	96	67	535	19.0	187	25.9	3.45	593	4.33	1.79	32	19.9	5.42
	09-MEN-14	30	17.1	101	165	66	76	532	18.8	199	27.4	4.01	583	4.52	1.86	28	19.5	5.54
	09-MEN-15	36	17.2	109	208	125	63	476	18.4	184	26.6	1.06	603	4.19	1.80	20	18.4	5.20
	10-MEN-73	35	15.9	91	148	71	82	544	20.6	212	29.4	6.25	629	5.09	2.18	38	24.6	6.42
Xenoliths	10-MEN-56	11	5.47	12.2	24	6	8.82	46	9.19	290	4.63	1.45	77	7.13	0.38	8	4.50	0.87
Xenoliths	10-MEN-59	21	2.28	7.7	8	*10*	30	57	11.0	277	5.07	0.47	153	6.93	0.42	8	6.47	1.37
Xenoliths	10-MEN-61x	30	7.13	2.2	13	3	101	220	12.9	31	10.5	2.58	260	1.16	1.59	36	2.05	5.01
Xenoliths	10-MEN-62	63	2.65	15.6	9	*10*	0.73	346	13.7	124	4.57	0.08	11.6	3.14	0.31	10	2.88	1.07
Xenoliths	10-MEN-72	16	4.99	8.5	20	4	7.01	7.91	3.41	453	4.74	0.58	20.7	11.7	0.37	2	6.30	1.14

Measured by LA-ICP-MS, except Ni (italic LA-ICP-MS), Cr and Pb, which were measured using XRF. All values are in ppm. Typical analytical uncertainties are given in Supplementary dataset 2.

Table 2: continued

	Sample name	La	Ce	Pr	Nd	Sm	Eu	Gd	Dy	Ho	Er	Yb	Lu
	10-MEN-50	39.0	68.8	7.8	30.2	5.73	1.45	4.78	3.64	0.70	1.87	1.81	0.28
	08-MEN-10	25.0	42.7	5.07	21.1	4.41	1.11	4.15	4.35	0.86	2.36	2.16	0.31
	10-MEN-52	41.3	71.4	8.2	32.3	5.94	1.51	4.96	4.08	0.78	2.16	1.94	0.29
	10-MEN-53	26.6	48.2	5.55	22.2	4.51	1.15	4.35	4.00	0.74	2.15	2.05	0.30
	10-MEN-54a	25.0	52.7	5.59	21.5	4.35	1.08	3.94	3.96	0.75	2.13	2.16	0.32
	10-MEN-55	25.3	51.3	5.6	21.8	4.27	1.12	4.15	3.66	0.74	1.98	2.00	0.28
	10-MEN-61h	34.7	65.6	7.34	28.3	5.42	1.45	4.81	4.01	0.78	2.11	1.99	0.29
	10-MEN-65	42.6	72.8	8.41	32.9	5.87	1.45	4.88	3.99	0.76	2.10	2.07	0.30
	08-MEN-09	42.6	68.9	8.14	33.4	6.19	1.48	5.20	4.37	0.82	2.22	2.05	0.30
	10-MEN-66	39.9	76.3	8.29	31.3	5.63	1.51	4.67	3.60	0.67	1.91	1.75	0.28
	08-MEN-05	32.3	54.7	6.49	26.5	5.22	1.35	4.8	4.23	0.83	2.27	2.13	0.33
	08-MEN-06a	73.8	119.7	12.56	44.6	6.68	1.41	5.61	4.22	0.80	2.18	2.00	0.29
	08-MEN-06b	30.0	57.1	6.51	25.3	5.02	1.33	4.47	3.78	0.72	2.00	1.87	0.26
	09-MEN-16	31.4	59.6	6.75	26.4	5.14	1.41	4.65	4.09	0.76	2.12	1.99	0.29
	10-MEN-67	36.6	72.0	7.76	29.5	5.51	1.37	4.62	3.79	0.71	2.04	1.91	0.29
	10-MEN-68	37.1	70.4	7.69	29.7	5.59	1.42	4.76	4.01	0.78	2.12	2.03	0.31
	10-MEN-69	40.3	76.6	8.38	31.5	5.87	1.48	4.58	3.65	0.69	1.85	1.79	0.25
	10-MEN-70	39.0	75.4	8.16	31.2	5.58	1.45	4.56	3.66	0.68	1.91	1.77	0.25
	10-MEN-71	45.2	84.1	9.17	34.6	6.35	1.51	5.17	4.29	0.80	2.26	2.07	0.30
	08-MEN-08	41.0	66.5	7.86	31.9	5.93	1.52	5.07	4.26	0.80	2.22	2.01	0.30
	09-MEN-11	41.7	79.1	8.52	32.6	6.0	1.51	4.79	3.91	0.73	1.98	1.86	0.28
	09-MEN-12	36.5	68.0	7.71	30.2	5.67	1.49	4.88	4.00	0.74	2.00	1.96	0.26
	09-MEN-13	39.3	70.5	7.86	30.7	5.52	1.52	4.76	3.85	0.70	1.99	1.89	0.27
	09-MEN-14	37.9	71.3	7.79	30.0	5.61	1.46	4.59	3.69	0.71	2.01	1.84	0.26
	09-MEN-15	36.5	70.1	7.82	30.1	5.71	1.50	4.69	3.71	0.71	1.94	1.73	0.26
	10-MEN-73	47.3	86.4	9.35	35.5	6.34	1.57	5.14	4.24	0.80	2.13	2.04	0.31
Xenoliths	10-MEN-56	11.4	22.9	2.55	10.2	2.02	0.34	1.84	1.63	0.33	0.97	1.01	0.17
	10-MEN-59	15.5	36.3	3.60	13.3	2.40	0.23	2.03	2.01	0.38	1.02	0.94	0.14
	10-MEN-61x	5.19	11.0	1.08	4.09	1.08	0.45	1.57	2.10	0.41	1.14	1.09	0.13
	10-MEN-62	13.2	30.0	3.03	12.1	2.62	0.59	2.52	2.37	0.47	1.22	1.09	0.15
	10-MEN-72	6.28	14.4	1.38	5.22	0.87	0.10	0.74	0.60	0.14	0.46	0.54	0.11

Measured by LA-ICP-MS. All values are in ppm. Typical analytical uncertainties are given in Supplementary dataset 2.

Table 3: Whole rock radiogenic isotope data for selected lamprophyre samples

SILL	sample	$^{87}Sr/^{86}Sr_{(m)}$	$^{87}Sr/^{86}Sr_{(i)}$	$^{143}Nd/^{144}Nd_{(i)}$	εNd	$^{206}Pb/^{204}Pb_{(m)}$	$^{207}Pb/^{204}Pb_{(m)}$	$^{208}Pb/^{204}Pb_{(m)}$	$^{206}Pb/^{204}Pb_{(i)}$	$^{207}Pb/^{204}Pb_{(i)}$	$^{208}Pb/^{204}Pb_{(i)}$	L-$^{87}Sr/^{86}Sr_{(m)}$	L-$^{87}Sr/^{86}Sr_{(i)}$
1	10-MEN-50	0.710793±3	0.71076	0.512501±4	-2.4	19.067	15.763	39.44	19.03	15.76	39.4	0.713039±3	0.71301
3	10-MEN-53	0.710673±8	0.71059	0.512557±5	-3.1	18.904	15.718	39.168	18.88	15.72	39.15	0.712551±4	0.71246
	10-MEN-54	0.708850±5	0.70862	0.512505±5	-3.2	18.913	15.723	39.186	18.88	15.72	39.17	0.710219±5	0.70999
	10-MEN-61h	0.706488±4	0.7064	0.512472±5	-2	18.935	15.714	39.168	18.91	15.71	39.14	0.708305±4	0.70822
6	10-MEN-66	0.709286±6	0.70918	0.512465±5	-2.3	19.052	15.74	39.362	19.02	15.74	39.33	0.710895±3	0.71079
	10-MEN-69	0.708321±3	0.70828	0.512528±5	-2.2	19.045	15.739	39.37	19.01	15.74	39.33	0.711150±2	0.71111
	10-MEN-70	0.708114±3	0.70806	0.512511±5	-2.7	19.022	15.72	39.29	18.99	15.72	39.26	0.710685±5	0.71063
9	08-MEN-08	0.706758±5	0.70667	0.512517±5	-2.5	19.017	15.741	39.345	19.01	15.74	39.33	0.707703±4	0.70761
	09-MEN-14	0.706168±4	0.70609	0.512491±6	-1.4	19.039	15.742	39.351	19.01	15.74	39.32	0.706757±4	0.70668
	10-MEN-73	0.706825±5	0.70674	0.512502±5	-2.5	19.031	15.741	39.358	19.01	15.74	39.33	0.707243±2	0.70716
xeno	10-MEN-56	0.713750±4	0.71364	0.511986±4	-12.6	18.887	15.701	39.326	18.87	15.7	39.3		
	10-MEN-59	0.711298±4	0.71099	0.511940±5	-13.5	19.032	15.756	39.359	19.01	15.75	39.32		
	10-MEN-61x	0.711055±6	0.71079	0.512278±6	-7	18.874	15.715	39.097	18.85	15.71	39.09		
	10-MEN-62	0.710651±3	0.71065	0.512223±4	-8	18.935	15.71	39.176	18.92	15.71	39.16	0.710652±3	0.71065
	10-MEN-72	0.707903±4	0.70739	0.511966±5	-12.9	19.294	15.753	39.839	19.21	15.75	39.69		

(m) = measured value after correction for mass fractionation (i) = initial value, recalculated to the estimated emplacement age of 15 Myr; Analytical uncertainties for Sr and Nd are given at 2sm level. For Pb, reproducibility at 2s level is better than 0.1%. L- leachate

Table 4: Results of the amphibole-based thermobarometry.

Sample number	**13**	**13**	**13**	**13**	**13**	**13**	**13**	**13**	**13**	**13**
Amphibole grain	**13_amph1**	**13_amph1**	**13_amph2**	**13_amph2**	**13_amph4**	**13_amph4**	**13_amph5**	**13_amph5**	**13_amph6**	**13_amph6**
Position	Core	Rim	Core	Rim	Core	Rim	Core	Rim	Core	Rim
SiO_2	42.04	42.42	40.89	42.11	41.76	41.98	41.74	43.91	41.92	42.03
TiO_2	2.79	3.52	3.52	4.12	3.34	3.41	3.37	3.45	3.28	4.03
Al_2O_3	11.80	11.03	12.89	10.57	11.88	11.13	12.29	9.33	12.14	10.59
Cr_2O_3	0.18	0.23	0.05	0.14	0.16	0.13	0.21	0.12	0.21	0.11
FeO*	9.36	10.02	9.53	10.56	10.25	11.48	8.64	10.67	9.10	10.73
MnO	0.12	0.14	0.14	0.18	0.15	0.17	0.11	0.16	0.12	0.14
MgO	15.42	14.73	14.62	14.23	14.52	13.61	15.50	14.69	15.05	14.19
CaO	10.97	11.18	10.93	11.18	11.14	11.03	10.98	11.08	11.02	11.08
Na_2O	2.39	2.43	2.48	2.46	2.41	2.40	2.46	2.21	2.36	2.43
K_2O	0.88	0.93	1.05	0.88	0.98	1.00	1.04	0.80	1.03	0.86
F	0.11	0.27	0.21	0.23	0.15	0.33	0.12	0.25	0.25	0.24
Cl	0.01	0.02	0.01	0.02	0.01	0.03	0.01	0.03	0.01	0.02
Mg#	0.75	0.72	0.73	0.71	0.72	0.68	0.76	0.71	0.75	0.70
Amphibole-only thermobarometry using equations from Ridolfi & Renzulli (2012)										
T (°C)	1027	986	1041	980	1031	954	1050	929	1040	971
error (°C)	22	22	22	22	22	22	22	22	22	22
P (MPa)	808	384	907	305	798	334	880	225	858	302
Eq.	P1e	P1b_c	P1e	P1b	P1e	P1b	P1e	P1b	P1e	P1b
error (MPa)	97	46	109	37	96	40	106	27	103	36
Depth (km)	31	15	34	12	30	13	33	9	32	11